DRAFT VERSION SEPTEMBER 1, 2026
Research in Astronomy and Astrophysics manuscript no.

FAST Pulsar Database: II. Scattering Profiles of 158 Pulsars

W. C. JING [1,2] J. L. HAN [1,2,3,*] C. WANG [1,2,3] P. F. WANG [1,2,3] T. WANG [1] N. N. CAI [1] J. XU [1,3] Z. L. YANG [1,2] D. J. ZHOU [1] YI YAN [1] W. Q. SU [1,2] X. Y. GAO [1] AND L. XIE [1]

[1] *National Astronomical Observatories, Chinese Academy of Sciences, Jia-20 Datun Road, ChaoYang District, Beijing 100012, China*
[2] *School of Astronomy and Space Science, University of Chinese Academy of Sciences, Beijing 100049, China*
[3] *State Key Laboratory of Radio Astronomy and Technology, Beijing 100101, China*

ABSTRACT

The turbulent ionized interstellar medium diffracts radio waves, causing them to propagate along multiple paths. The pulse-broadening observed at low frequencies results from scattering by interstellar ionized gas clouds. During the Galactic Plane Pulsar Snapshot (GPPS) survey and other projects using the Five-hundred-meter Aperture Spherical radio Telescope (FAST), we detect pulse broadening for 158 pulsars in the radio frequency band between 1.0 and 1.5 GHz, including 71 newly discovered pulsars in the GPPS survey and 87 previously known pulsars. We find that a more accurate dispersion measure can be obtained by aligning the front edge of the scattered subband pulses at the 1/4 or 1/2 peak level for most pulsars with a single dominant component in the intrinsic profile, and by using the best DM values from aligning the intrinsic profile components in the model fit. From the pulse profiles at a few subbands, we derive the pulse-broadening timescale and the scattering spectral index. These scattering parameters are measured for the first time for 121 pulsars. For 37 pulsars with previously detected scattering features, our measurements of the pulse-broadening timescale are consistent with results in the literature. We find that pulsars behind spiral arms exhibit stronger scattering due to greater density fluctuations in the arm regions. With a properly derived dispersion measure and careful calibration, we also present polarization profiles for 82 pulsars in three subbands of FAST observations.

Keywords: pulsars: general — ISM: scattering — Galaxy: general

1. INTRODUCTION

Ionized gas in the interstellar medium can cause two kinds of effects when radio pulses from pulsars pass through. One is the dispersion effect on pulses, which causes longer delays at lower frequencies. The more electrons accumulated along the path, the larger the pulse delay. The dispersion measure (DM) for pulses is thus defined as $DM = \int_{\rm psr}^{\rm us} n_e(l)\mathrm{d}l$, in units of pc cm^{-3}. Here $n_{\rm e}(l)$ is the electron density at a distance l in units of cm^{-3}, and $\mathrm{d}l$ is the unit length along the line of sight in pc. The distribution of electron density in the Milky Way can be described by the NE2001 model (Cordes & Lazio 2002) and the YMW16 model (Yao et al. 2017). For most pulsars without distance measurements, their distances can be estimated from observed DM values using models. The second effect is the scattering caused by the irregular distribution of ionized gas clouds, which leads to multipath propagation of radio waves (Scheuer 1968) and is shown by the angular broadening of the point source, the intensity scintillation in the frequency and time domain, and the pulse broadening (see Rickett 1977, 1990, and references herein).

The scattering effect broadens the intrinsic narrow pulses asymmetrically, so that the scattered profile can be expressed by the convolution of the intrinsic profile with a pulse broadening function (PBF) (Staelin 1970):

$$\mathrm{PBF}(t) = \tau_{\rm s}^{-1}\exp(-t/\tau_{\rm s})U(t) \quad (1)$$

where $\tau_{\rm s}$ represents the pulse-broadening timescale, and $U(t)$ is the Heaviside step function (Bhat et al. 2004). This PBF assumes a thin screen in the middle between the pulsar and the observer (Cronyn 1970). The thin-screen model is generally used to describe the interstellar scattering (e.g. Cordes et al. 1985; Oswald et al. 2021). The pulse-broadening timescale $\tau_{\rm s}$ depends on the observing frequency ν, and is typically described by a power-law relation (e.g. Bernadich et al. 2024):

$$\tau_{\rm s}(\nu_{\rm GHz}) = \tau_{\rm 1GHz}\cdot\nu_{\rm GHz}^{-\alpha} \quad (2)$$

where α is the scattering spectral index.

Previously, Löhmer et al. (2001) and Li & Han (2003) used the unscattered profile at high frequencies as the intrinsic profile to measure or model pulse broadening at lower frequencies. Lewandowski et al. (2015b) allows the possible evolution of the profile components with frequency and then fits the data to determine $\tau_{\rm s}$. Nice et al. (2013) simultaneously fit the intrinsic profile, pulse-broadening timescale at 1 GHz and DM by assuming $\alpha = 4$. Fonseca et al. (2024) tried to fit pulse profiles in the 2-D frequency-time waterfall plot for fast radio bursts and radio pulsars. The pulse-broadening

* E-mail: hjl@nao.cas.cn

timescale τ_s at 1 GHz, $\tau_{1\rm GHz}$, and the scattering spectral index α are two conventional characteristic parameters to describe the scattering effect. For Kolmogorov turbulence, one should obtain $\alpha = 4.4$ (Rickett 1990). For the Gaussian turbulence, $\alpha = 4.0$ (e.g. Lee & Jokipii 1975a,b). The α derived from observations typically has a value around 4.0 with a deviation of about 0.6 (Oswald et al. 2021).

The pulse-broadening timescale τ_s is related to observed DMs of pulsars. It varies with $\rm DM^{2.2}$ for the turbulent density distribution with a Kolmogorov spectrum, or $\rm DM^{2.0}$ for the medium with a Gaussian spectrum (Rickett 1977). The DM dependence is not linear, and the observed $\tau_s - \rm DM$ relation shows a steeper slope at high DM values than $\rm DM^{2.2}$ (e.g. Sutton 1971; Bhattacharya et al. 1992; Ramachandran et al. 1997). Considering the frequency dependence and DM dependence together, one can get a joint empirical formula, e.g.

$$\log(\tau_s) = a + b(\log DM) + c(\log DM)^2 - \alpha \log \nu_{\rm GHz} \quad (3)$$

by Bhat et al. (2004), where $a = -6.46$, $b = 0.154$, $c = 1.07$ and $\alpha = 3.86 \pm 0.16$, or

$$\tau_{1\rm GHz} = 1.9 \times 10^{-7} {\rm ms} \times DM^{1.5} \times (1 + 3.55 \times 10^{-5} DM^3) \quad (4)$$

by Cordes et al. (2022). The data are scattered from this relation by 0.76 dex. The slope against DM becomes slightly steeper at higher DM due to the large density fluctuations in the inner Galaxy (Xu & Zhang 2017; Dexter et al. 2017; Cordes et al. 1985, 2016). Observed values of τ exhibit a spread of about two orders of magnitude around the empirical curves (Cordes et al. 2022). This is because of various fluctuations (Ocker & Cordes 2026). On the one hand, there are large-scale electron density fluctuations distributed in the Galactic disk, halo, and spiral arms. On the other hand, there are small-scale density fluctuations caused by supernova shocks, stellar winds, and HII regions (Taylor & Cordes 1993; Cordes & Lazio 1997, 2001, 2002, 2003; Ocker et al. 2021; He et al. 2025; Patil et al. 2026).

The scattering effect not only broadens the pulse profile but also redistributes the polarized emission into profile tails. The polarization profiles can be explained as the original profiles convolved with the PBF (Komesaroff et al. 1972). As a result, the polarization position angle (PA) curve tends to be flattened for the exponential tail of the profile (Li & Han 2003). This has been further verified by additional observations (e.g., Karastergiou 2009), including the data presented in this paper.

Currently, the Five-hundred-meter Aperture Spherical radio Telescope (FAST) (Nan 2006; Nan et al. 2011) is the most sensitive telescope in the world. Since 2019 it has been working on many pulsar projects, including the Galactic Plane Pulsar Snapshot (GPPS) survey (Han et al. 2021). Up to now, more than 851 new pulsars have been discovered by this survey (Han et al. 2021, 2024). FAST has also been used for many related pulsar studies, such as the polarization measurements of 682 pulsars (Wang et al. 2023), the HI absorption measurements of a pulsar (Jing et al. 2023), detection of dwarf pulses (Chen et al. 2023b; Yan et al. 2024), observations for mode-changing of pulsars (Yan et al. 2023), and pulsar timing (Su et al. 2023).

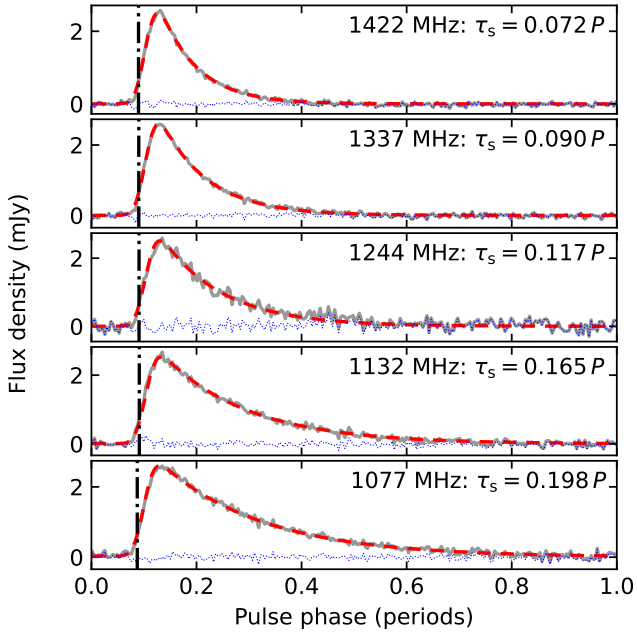


Figure 1: An example of fitting scattered features for sub-band profiles of FAST observations. The observed profiles (solid grey line) for PSR J2052+4421g are presented for 4 subbands. The fitted (dashed) profiles are obtained by convolving a Gaussian with the standard PBF. The central frequencies and pulse-broadening timescales, expressed as fractions of the pulsar period, are marked in each subpanel of the sub-band profile.

This paper presents the database of scattering profiles for 158 pulsars observed by the FAST during the FAST GPPS survey (Han et al. 2021, 2024) and other projects by the co-authors (e.g. Xu et al. 2022). Among them, 71 pulsars were discovered by the GPPS survey. Section 2 describes the FAST observations and data processing, including a method to get better DM values from the scattered signals than those from conventional routines. Section 3 presents the results and relevant discussion. Conclusions are given in Section 4.

2. FAST OBSERVATIONS AND DATA PROCESSING

All observations have been carried out by using the FAST L-band 19-beam receiver (Jiang et al. 2020), which works in the radio band of 1.0 – 1.5 GHz. The digital bands can record the 4 (XX, YY, Re[X^*Y] and Im[X^*Y]) or 2 (XX, YY) polarization channel data for all 2048 frequency channels covering the band with a sampling time of 49.152 μs. Polarimetric calibration is achieved using the amplitude-modulated noise signals with a period of 2.01326592 s and a duty cycle of 50% (Wang et al. 2023).

The folding of pulsar data and polarimetric calibration were processed in the following steps. Data from frequency channels at the lower edge, covering a 45 MHz band, and

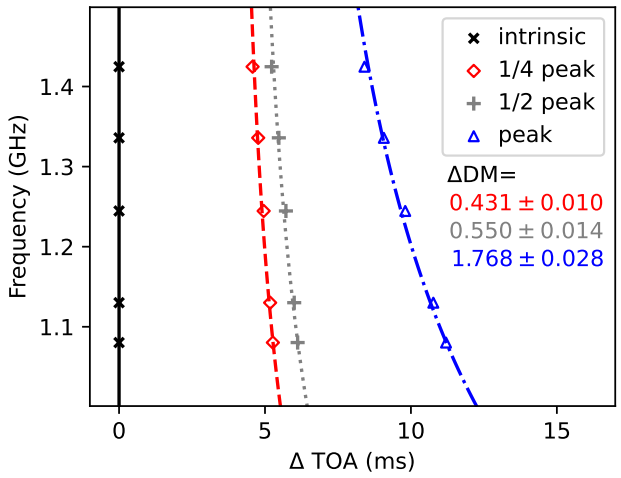


Figure 2: TOA delays for subband profiles for PSR J2052 +4421g measured by using the DM values from aligning the peak, the lead edge at the half peak level (1/2), and at the quarter peak level (1/4), compared to TOA from the exactly de-convolved intrinsic profile component alignment without scattering delay. There is a small DM offset caused by different alignments, depending on the pulsar period, as indicated inside a plot.

at the higher edge, covering a 30 MHz band, have been discarded due to low gains (Jiang et al. 2020). The data are first folded into a pulse stack by using *DSPSR* (van Straten & Bailes 2011), based on the pulsar ephemeris from the Pulsar Catalog (Manchester et al. 2005). For pulsars without timing solutions, we use *PDMP* from PSRCHIVE[1] (Hotan et al. 2004) to get the best pulsar period. Radio frequency interference (RFI) in some channels is mitigated manually by using *PAZ* (van Straten et al. 2012) or automatically by using the new tool $2\sigma CRF$ (Chen et al. 2023a).

When a pulsar is strongly scattered, the pulse is much more broadened at lower frequencies. Ideally, profiles with high signal-to-noise ratios from very fine frequency channels over a wide frequency range are needed to fit the scattering model. In practice, a compromise has to be made on the bandwidth and signal-to-noise ratio. In practice, we measure the scattering parameters using 3 to 5 subband profiles from FAST pulsar observations, depending on signal strength and RFI conditions, and then use the 32-subband data to verify the results.

2.1. *Preliminary determination of DM from scattering profiles*

Obtaining unbiased DM measurements can be rather difficult for highly scattered pulsars. An incorrect DM value can lead to the misalignment of scattering profiles. The conventional method for measuring pulsar DM is to align the pulse peaks of all subband profiles. For broadened pulses

[1] http://psrchive.sourceforge.net

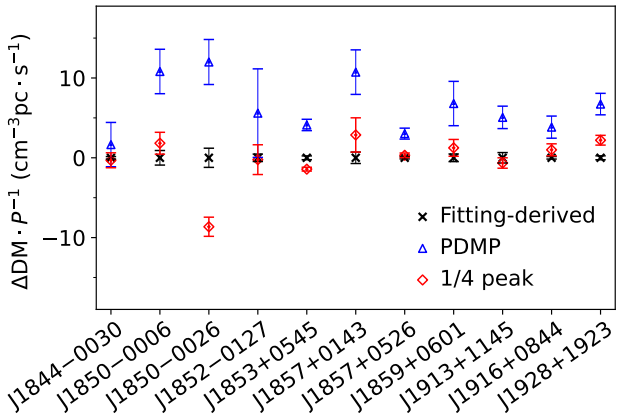


Figure 3: Comparison of DM estimates derived by using three alignments: DM values in the 2-D fitting (Oswald et al. 2021), the DM value directly measured by the *PDMP* tool (based on the peak alignment), and the DM value from the front-edge alignment at the 1/4 peak level.

with shifted peaks at lower frequencies (Oswald et al. 2021), this method introduces a large systematic deviation in the real DM value.

To minimize the DM bias, some new methods have been proposed, either through fitting profiles based on specific assumptions (Geyer et al. 2017; Andersen et al. 2023) or by using data-driven methods that avoid excessive assumptions about PBFs and intrinsic profiles (e.g. Hessels et al. 2019). For pulsars with a single dominant component scattered with the pulse broadening function of an exponential function given by the thin screen discussed above, we can get a DM by straightforwardly aligning the leading edge at a half (1/2) or a quarter (1/4) level of the peak, as demonstrated in Fig. 1. This method was first presented by Ables et al. (1970). We evaluate possible DM offsets from different alignments of the scattered profile of PSR J2052+4421g, a newly discovered pulsar in the FAST GPPS survey. To remove white noise from subband profiles, we simultaneously fit the pulse-broadening timescale at 1 GHz $\tau_{1\mathrm{GHz}}$ and the scattering spectral index α, assuming the same intrinsic profile across the observing band, similar to Nice et al. (2013).

The observed and fitted subband profiles are aligned well in Figure 1. Using these scattering parameters, we generate a noise-free waterfall plot that can reveal the frequency-dependent times of arrival (TOAs) for the half- and quarter-level alignment of the front edges and the peak positions for all subband profiles, with an example shown in Figure 2, which in fact cause different systematic DM deviations. Taking the DM values from the careful 2-D fitting method (Oswald et al. 2021) as the reference, we compare the DM values obtained from the normal *PDMP* in the PSRCHIVE package and the 1/4 peak level alignment, as shown in Fig. 3, and find that the DM values obtained by the 1/4 peak alignment are much better than those obtained by the *PDMP* and the offset is almost ignorable if the intrinsic profiles and PBFs are properly assumed.

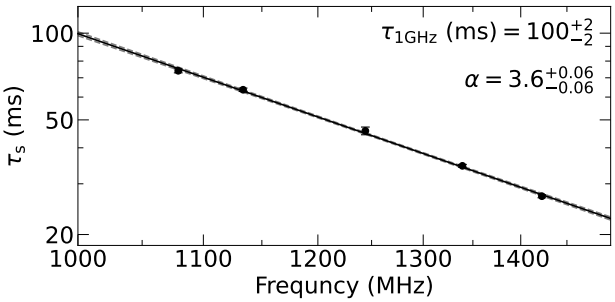


Figure 4: Fitting the pulse-broadening timescale τ_s to get the scattering spectral index α. The pulse-broadening timescales are obtained from Fig. 1 using the technique described in Section 2.2.1. From such a power-law fitting, one can get the frequency dependence of τ_s and α (with the $\pm 1\sigma$ uncertainties).

2.2. *Jointly fitting subband profiles for DM and scattering parameters*

The DM of a scattered pulsar, preliminarily obtained by aligning the leading edges of subband profiles at the half- or quarter-peak power level, can be used to further jointly fit the DM-corrected subband profiles for the pulse-broadening timescale and a new DM iteratively.

There are four methods in literature to get the pulse-broadening timescale from the scattering profiles: (1) directly fitting the observed profiles using the convolution of the best-trial intrinsic profile and the PBF (e.g. Cordes et al. 1985; Kuzmin & Losovsky 2007); (2) the deconvolution of the scattering profiles by using the "CLEAN" method (e.g. Bhat et al. 2003; Young & Lam 2024; Bathula et al. 2026); (3) the deconvolution of the profiles in the Fourier domain (Kuz'min & Izvekova 1993); (4) the coherent cyclic spectral analysis to resolve the frequency-dependent time delay due to multipath propagation from base-band data (e.g. Demorest 2011). The last method works on the base-band data, which is not applicable here. The deconvolution method and the clean method can work well on subband profiles with high signal-to-noise ratios (S/Ns), whereas our subband profiles do not always have high S/Ns. Because our subband profiles span a wide range of signal-to-noise ratios, we use the direct fitting method and acknowledge potential parameter bias arising from the assumed intrinsic profile. Fortunately, most pulsars have one dominant profile component, or two or three components that can be easily identified from the highest-frequency subband profile. The thin screen model can describe the scattering medium for most pulsars.

We fit subband profiles for the typical pulse-broadening timescale at 1 GHz, the scattering spectral index α and the model DM iteratively. The details are outlined below.

2.2.1. *Fitting the subband profiles independently*

The pulse-broadening timescale τ_s in each subband can be directly obtained from the fitting on each subband profile (Geyer et al. 2017; Oswald et al. 2021). Then, one could get the scattering spectral index α from these fitted timescales for these subbands.

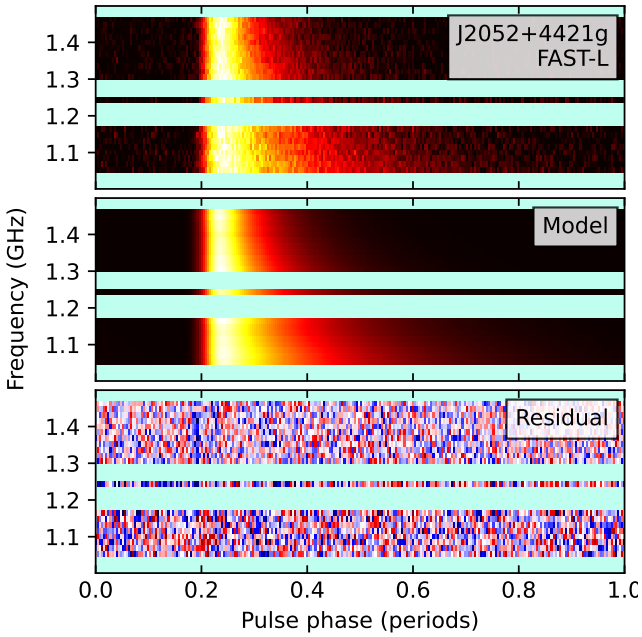


Figure 5: Comparison with the observed 32-subband data by the FAST (top panel) with the modeled profiles (middle panel) produced by the fitted scattering parameters. The scattering parameters should have been reasonably obtained if the residual image (bottom panel) is random and has no obvious structure. Here is only an example for PSR J2052+4421g, and some channels with RFI have been discarded. Comparisons for all pulsars are presented in Fig. A1.

The observed subband profiles are modeled as the convolution of the intrinsic profile, the PBF, and also the instrumental smearing function. The intrinsic profile is assumed to be a sum of multiple Gaussian components, $\Sigma G(t)$ (Kramer 1994), where t is the pulse phase. Each Gaussian component has three free parameters: amplitude A, center phase μ, and the characteristic width σ (Oswald et al. 2021). The number of Gaussian components is initially obtained from the subband profile at the highest frequency suffering the least scattering effect, and we limit the number to no more than 3 components to avoid over-fitting (Bansal et al. 2019). The PBF is modeled as an exponential decay as in Equation 1, representing the interstellar medium scattering effect (Löhmer et al. 2001, 2004). Instrumental smearing effects (Voûte et al. 2002) are described by the rectangular functions representing intra-channel dispersion $D(t)$ and sampling time $S(t)$. Thus, the scattered profile of each subband is then modeled by

$$I(t) = S(t) \otimes D(t) \otimes \mathrm{PBF}(t) \otimes \Sigma G(t), \qquad (5)$$

here, $\otimes$ denotes the convolution. A flat baseline is included for cases where the scattering tail is sufficiently long to spread energy across the entire phase of pulsar rotation (Geyer & Karastergiou 2016). The subband profiles from different subbands are fitted independently using the differ-

Table 1: Fitted scattering parameters for 156 pulsars derived from FAST observations

PSR Name	l	b	P	FAST Obs. Date	$T_{\rm obs}$	$\rm DM_{1/4}$	DM	$\tau_{\rm 1GHz}$	α
	(°)	(°)	(ms)	yyyy-mm-dd	(s)	($\rm cm^{-3}pc$)	($\rm cm^{-3}pc$)	(ms)	
(1)	(2)	(3)	(4)	(5)	(6)	(7)	(8)	(9)	(10)
J0248+6021	136.902	0.697	217.12	2023-08-14	1100	369.7(2)	369.6(2)	34.7(3)	3.91(3)
J1822−1252	18.218	0.394	2070.94	2026-04-28	600	885(9)	891(4)	185(3)	3.8(3)
J1822−1400	17.252	−0.176	214.75	2026-04-24	900	649.5(8)	649.3(9)	6.7(1)	3.27(8)
J1823−11	19.299	0.662	286.18	2026-08-14	900	743(5)	746(2)	103(13)	1.8(6)
J1823−1312g	18.024	0.044	381.03	2026-08-06	900	753(7)	757(3)	126(5)	3.0(2)
J1823−1344g	17.563	−0.200	467.66	2026-03-29	900	1101(26)	1099(2)	97(8)	4.1(4)
J1823−1347	17.488	−0.189	617.11	2026-03-29	900	1043.0(11)	1042.6(8)	36.3(7)	3.4(1)
J1824−1118	19.809	0.741	435.79	2025-08-18	900	601.5(2)	601.3(2)	28.20(7)	3.890(9)
J1829−1132g	20.202	−0.496	244.78	2026-04-19	900	849(3)	848.5(7)	35(4)	4.3(4)
J1831−1127g	20.468	−0.843	1402.86	2026-04-27	600	524(4)	525.0(11)	36(4)	2.9(4)
J1833−0204g	29.022	3.050	4.43	2021-10-18	900	312.1(1)	312.08(4)	0.8(1)	3.2(7)
J1833−0556	25.623	1.232	1521.63	2025-08-07	900	450(4)	453(4)	167(5)	2.98(10)
J1833−0559	25.514	1.321	483.50	2025-08-07	900	346(1)	347(1)	169(6)	3.5(2)
J1834−0602	25.640	0.965	487.96	2025-10-23	900	442.5(6)	440.7(2)	22.8(4)	5.65(10)
J1834−0633	25.173	0.763	317.32	2026-08-18	600	692(8)	687(4)	375(10)	4.06(9)
J1834−0812	23.709	0.001	491.19	2025-10-21	900	1125(13)	1136(7)	267(40)	1.8(5)
J1835−0643	25.093	0.553	305.87	2026-08-18	600	465.0(5)	464.8(4)	110(2)	3.81(6)
J1837−0604	25.960	0.265	96.31	2020-10-10	600	454.4(5)	455.5(3)	50(2)	5.4(1)
J1838−0453	27.070	0.708	380.96	2025-09-11	600	615.6(4)	615.6(3)	25.9(5)	4.60(8)
J1838−0508g	26.920	0.464	263.05	2026-01-03	900	786(3)	785.8(10)	43(3)	3.8(3)
J1840−0442g	27.504	0.251	155.46	2026-08-01	900	696(3)	703(2)	54(5)	3.4(3)
J1840−0445	27.486	0.203	422.35	2026-07-21	600	365(3)	366.6(11)	213(13)	3.4(2)
J1840−0643	25.662	−0.567	35.58	2020-08-13	600	493(1)	494.0(6)	26(2)	3.8(2)
J1841−0157	30.099	1.216	663.38	2021-09-01	900	473.4(3)	473.5(4)	14.44(6)	3.50(2)
J1841−0353g	28.375	0.359	778.64	2025-03-04	900	948(4)	949(2)	104.5(9)	2.99(9)
J1842−0153	30.283	1.022	1054.32	2026-08-22	900	423.9(5)	422.0(2)	32.9(2)	3.93(3)
J1842−0258g	29.202	0.738	596.30	2023-10-26	900	355.7(9)	355.7(7)	20.7(5)	3.7(1)
J1842−0309	29.077	0.584	404.95	2023-10-26	900	943.6(17)	948(1)	82(3)	3.8(2)
J1842−0415	28.086	0.111	526.68	2026-08-08	600	181.9(5)	181.5(4)	17.57(3)	5.0(7)
J1843−0050	31.295	1.360	782.66	2021-10-09	900	511.6(7)	511.6(4)	15.5(3)	3.61(6)
J1843−0137	30.543	1.087	669.88	2021-09-23	900	483.3(6)	483.4(8)	25.5(3)	3.53(4)
J1843−0157g	30.294	0.847	508.90	2021-08-22; 2021-09-03	1200	751(2)	751(2)	110(5)	3.4(2)
J1843−0310g	29.163	0.381	285.15	2024-06-16	900	1281(6)	1283(2)	222(19)	5.5(3)
J1843−0355	28.484	0.056	132.31	2021-05-28	300	794(2)	794.06(9)	38.4(3)	5.16(9)
J1844−0030	31.710	1.271	641.15	2020-04-21	900	603.1(7)	603.0(7)	11.0(2)	3.19(5)
J1844−0136g	30.685	0.843	417.27	2024-04-21	900	901(4)	903(2)	73(7)	4.2(3)
J1844−0142g	30.587	0.847	348.74	2021-09-23; 2021-10-18; 2021-11-11	2100	794.5(15)	794.4(9)	28(2)	4.9(2)
J1844−0202g	30.269	0.720	761.45	2023-02-18	900	628(6)	628(6)	64(7)	4.5(5)
J1844−0240	29.804	0.254	581.55	2022-11-20	300	315(5)	315(3)	64(5)	3.3(3)
J1844−0244	29.727	0.235	507.72	2022-11-20	300	422.0(6)	422.0(6)	20.3(3)	3.48(5)
J1844−0256	29.574	0.119	273.00	2022-11-20	300	819(2)	820.0(7)	98(5)	3.8(2)
J1844−0302	29.395	0.243	1198.63	2022-11-20	300	542(2)	542(2)	29(2)	4.4(3)
J1844−0310	29.343	0.036	525.02	2021-02-21	600	827(2)	827.8(7)	73(4)†	4.1(2)†
J1844−0502	27.670	−0.769	335.16	2026-07-12	600	315.4(12)	315.0(9)	65.0(5)	3.7(1)
J1844−0538	27.073	−0.941	255.73	2025-09-26	600	410.9(3)	410.7(2)	11.92(13)	4.06(6)
J1845−0103g	31.272	0.847	99.07	2021-10-22; 2021-11-11	1200	750.1(6)	750.6(2)	34(1)	4.46(10)
J1845−0142g	30.734	0.593	126.19	2022-01-20; 2022-01-30	1200	564(4)	563.1(6)	52(12)	3.1(7)
J1845−0144g	30.709	0.466	593.94	2021-12-25; 2022-01-13; 2022-01-30	2100	937.7(14)	937.7(14)	216(5)	4.14(8)
J1845−0229Ag	30.024	0.212	657.72	2022-11-27	900	832(5)	842(4)	238(22)	4.6(3)
J1845−0229Bg	30.098	0.085	463.05	2023-05-30	900	846(31)	876(7)	234(65)	5.1(9)
J1845−0243g	29.828	0.066	345.26	2023-05-26	900	747(4)	750(2)	191(24)	5.1(5)
J1845−0254g	29.677	−0.012	492.65	2023-07-06	900	735(35)	769(7)	516(74)	4.7(5)
J1845−0316	29.391	−0.255	207.64	2025-04-11	300	495.1(4)	495.1(3)	21(1)	5.1(2)
J1846−0211g	30.391	0.166	788.17	2022-09-02	900	838(3)	838(4)	114(8)	5.1(3)
J1846−0513	27.682	−1.207	23.38	2025-09-21	1280	310.32(7)	310.33(4)	2.07(6)	4.8(2)
J1848−0055	31.797	0.171	274.58	2021-10-24	300	1155(2)	1157.8(14)	119(9)	4.0(3)
J1849−0013	32.501	0.338	491.75	2020-08-15	900	343.6(9)	345.1(6)	71(3)	4.2(2)
J1849−0040	32.075	0.198	672.54	2021-01-30; 2021-11-11	1200	1265(4)	1265(4)	278(13)	4.9(2)
J1849−0200g	31.000	0.600	326.76	2022-06-11	900	883(4)	887(3)	160(33)	2.3(6)
J1849−0120g	31.491	−0.113	825.84	2024-01-03	7920	1045(30)	1067(8)	239(14)	1.8(3)

... to be continued.

Table 1: *– continued*

PSR Name	l	b	P	FAST Obs. Date	$T_{\rm obs}$	$\rm DM_{1/4}$	DM	$\tau_{\rm 1GHz}$	α
	(°)	(°)	(ms)	yyyy-mm-dd	(s)	($\rm cm^{-3}pc$)	($\rm cm^{-3}pc$)	(ms)	
(1)	(2)	(3)	(4)	(5)	(6)	(7)	(8)	(9)	(10)
J1850−0002	32.823	0.356	893.35	2022-11-06	3400	537(4)	537(2)	42(1)	3.4(1)
J1850−0006	32.764	0.093	2191.30	2020-02-23; 2020-08-21	1200	632(2)	629(3)	229(3)	3.70(4)
J1850−0020	33.081	0.453	1574.70	2021-01-30; 2020-04-01; 2020-04-02; 2020-08-01;	3900	598(2)	598(2)	34(1)	3.6(2)
J1850−0026	32.407	0.066	166.64	2020-04-02; 2020-08-01; 2020-08-19	2700	947.0(2)	947.5(2)	35.6(4)†	4.19(4)†
J1850−0031	32.369	0.041	734.15	2020-04-02; 2020-08-01; 2020-08-19	2700	895.0(16)	895(2)	105(2)	4.68(5)
J1850−0050g	32.103	−0.170	221.54	2021-09-03; 2021-10-09	1800	1060(4)	1064(2)	157(9)	4.3(2)
J1850+0242	35.265	1.403	4.48	2020-12-22	300	539.7(8)	539.7(2)	5.9(7)	4.8(4)
J1851−0029	32.542	0.335	518.68	2021-02-11; 2021-03-06	600	519.5(3)	519.5(3)	13.3(2)	3.42(5)
J1851−0108g	31.883	−0.466	87.09	2021-09-23; 2021-10-05	1200	669.6(6)	669.6(4)	25(2)	4.6(3)
J1851−0241	30.515	1.186	435.19	2022-11-22	300	511(3)	511(2)	105(9)	4.1(3)
J1851+0233	35.181	1.232	344.02	2020-05-28	300	606(8)	610(3)	84(18)	4.1(7)
J1852−0127	31.706	−0.802	429.01	2021-09-01	300	427.7(7)	427.9(9)	66.2(8)	3.89(4)
J1852+0013	33.282	0.174	957.75	2020-04-17; 2020-08-11; 2020-08-17; 2020-09-20	3600	542.7(3)	542.7(3)	21.3(2)	3.63(4)
J1852+0018	33.326	−0.085	318.77	2019-08-25; 2020-04-17; 2020-09-15	2100	452.9(7)	452.9(8)	20(2)	3.7(3)
J1852+0031	33.523	0.017	2180.47	2020-08-16; 2021-11-14	1800	752.0(15)	745.6(13)	803(2)	3.720(8)
J1852+0056g	33.864	0.254	1177.91	2020-04-04; 2020-08-19; 2020-08-20; 2020-09-11; 2020-11-06; 2021-02-07; 2022-02-07	6300	893.4(12)	893.6(15)	118(3)	4.82(8)
J1852+0309g	35.821	1.271	5.58	2021-03-06	900	358.0(4)	358.18(6)	3.6(6)	4.3(7)
J1853−0049g	32.389	−0.731	16.78	2022-05-09	900	405.4(4)	405.6(2)	5.4(12)	3.8(8)
J1853−0054g	32.421	−0.974	308.35	2021-12-21; 2022-01-13	1200	441.6(6)	441.6(8)	17(1)	4.0(2)
J1853+0237g	35.552	0.635	427.36	2020-04-19; 2021-03-20	1200	715(7)	718(2)	78(9)	4.5(5)
J1853+0505	37.650	1.956	905.06	2021-04-22	300	263.0(5)	260.4(6)	209(1)	3.60(2)
J1853+0545	38.353	2.064	126.41	2020-08-01	300	197.72(3)	197.73(4)	20.9(1)	3.89(2)
J1854−00	33.849	−0.394	716.87	2020-04-20	300	492(2)	491.7(17)	18.0(5)	2.8(1)
J1854+0131g	34.647	0.000	2043.73	2020-02-17; 2020-08-17; 2020-09-10; 2020-10-05	3000	451(8)	450(8)	607(27)	3.0(2)
J1855−0221g	31.345	−2.076	2.77	2023-03-05	900	223.25(7)	223.32(4)	0.8(2)	4.4(7)
J1855+0205	35.281	0.007	246.83	2019-09-13	300	866.1(8)	866.1(6)	17.8(3)	3.4(2)
J1855+0422	37.314	1.052	1678.11	2020-12-04	300	453.9(9)	449(1)	50.5(9)	4.60(8)
J1855+0455g	37.753	1.398	101.01	2020-08-13	900	372(2)	372.0(5)	21(2)	3.8(4)
J1855+0511g	37.985	1.534	1421.47	2024-02-17	900	285(2)	284.7(18)	160(4)	3.72(10)
J1855+0527	38.227	1.642	1393.47	2020-04-19	300	353(3)	353(3)	99(4)	3.9(2)
J1856+0245	36.007	0.057	80.91	2020-11-04	600	621(2)	619.1(6)	29(4)	4.9(6)
J1857+0143	35.168	−0.571	139.79	2019-09-17	300	248.5(4)	248.3(2)	41.5(9)	3.39(8)
J1857+0210	35.586	−0.393	630.97	2021-11-07	300	778.8(6)	778.9(8)	32.0(9)	4.6(2)
J1857+0214	35.577	−0.241	333.92	2020-02-12; 2020-08-22	1800	972(12)	982(7)	196(43)	2.7(7)
J1857+0300	36.274	0.072	772.68	2020-05-20	300	690(2)	690(2)	18(2)	4.9(4)
J1857+0526	38.438	1.187	349.96	2020-05-14; 2021-08-26	1800	464.85(10)	465.1(1)	24.0(3)	3.82(4)
J1858+0215	35.725	−0.493	745.76	2020-04-19	300	697(1)	697(1)	42(2)	3.1(2)
J1858+0244g	36.122	−0.212	2.61	2021-12-10	900	282.45(4)	282.57(3)	1.6(2)	5.3(5)
J1859+0430	37.819	0.343	336.32	2020-04-02	900	780(4)	780(2)	24(3)	4.0(6)
J1859+0601	39.245	0.903	1044.24	2020-03-04; 2020-08-21	1500	273.5(11)	273.8(13)	68(3)	2.9(2)
J1900+0438	38.067	0.169	312.29	2020-04-04; 2020-08-15	1800	622(4)	623(3)	193(17)	4.8(3)
J1901+0300	36.811	−0.974	7.80	2020-10-28	1670	253.70(2)	253.69(2)	0.52(1)	3.52(8)
J1901+0459	38.490	0.087	877.07	2020-12-19	600	1100(6)	1100(5)	121(12)	4.8(4)
J1902−0107g	33.211	−2.996	6.12	2022-07-21	900	290.2(2)	290.02(8)	2.6(3)	3.4(5)
J1903+0327	37.336	−1.014	2.15	2020-05-23	900	297.526(9)	297.533(4)	0.45(3)	4.3(5)
J1905+0600	39.838	−0.277	441.25	2020-02-19	300	727.1(5)	727.1(5)	19.7(2)	3.80(4)
J1907+0534	39.717	−0.988	1138.32	2020-05-14	300	522.7(7)	522.7(7)	20.5(4)	3.41(9)
J1908+0833	42.469	0.171	512.15	2020-10-26	300	698(2)	698(2)	35(2)	4.6(3)
J1908+0839	42.560	0.229	185.41	2020-10-26	600	513.3(2)	513.3(3)	8.9(1)	2.75(5)
J1908+0909	42.972	0.494	336.55	2019-12-26	300	465.3(2)	465.3(2)	7.4(2)	2.36(6)
J1910+0534	40.056	−1.668	452.85	2021-06-21	300	478.2(5)	478.2(6)	14.4(2)	2.97(5)
J1910+1026	44.438	0.504	531.59	2020-09-01; 2020-11-23	1200	714.0(12)	713.9(13)	23(2)	3.3(2)

... to be continued.

Table 1: – *continued*

PSR Name	l	b	P	FAST Obs. Date	$T_{\rm obs}$	$\rm DM_{1/4}$	DM	$\tau_{\rm 1GHz}$	α
	(°)	(°)	(ms)	yyyy-mm-dd	(s)	($\rm cm^{-3}pc$)	($\rm cm^{-3}pc$)	(ms)	
(1)	(2)	(3)	(4)	(5)	(6)	(7)	(8)	(9)	(10)
J1911+0101A	36.111	−3.918	3.62	2021-11-19	750	202.54(2)	202.56(1)	0.42(1)	3.38(10)
J1911+0925	43.675	−0.220	323.87	2020-08-06	900	481(3)	481(2)	48(7)	4.0(5)
J1913+1000	44.285	−0.194	837.16	2021-01-13	900	420.9(7)	420.3(6)	17.0(3)	2.90(6)
J1913+1102	45.250	0.194	27.27	2022-05-02; 2022-06-20	6000	338.83(5)	338.91(4)	11.6(2)	4.15(6)
J1913+11025	45.286	0.127	923.90	2025-08-23	900	620(2)	620(2)	47(2)	2.5(2)
J1913+1145	45.920	0.476	306.05	2020-05-23	300	641.9(2)	641.9(2)	15.9(2)	4.19(5)
J1914+1054g	45.213	−0.000	138.87	2020-12-28	900	417.6(6)	417.6(7)	12(2)	4.0(6)
J1916+0844	43.538	−1.493	440.02	2020-12-15	300	338.6(2)	338.5(3)	12.27(8)	3.34(3)
J1918+1340g	48.197	0.254	232.98	2020-08-07	900	572.6(4)	572.6(3)	26.3(7)	4.6(2)
J1919+1314	47.895	−0.088	571.45	2021-10-12	300	612.4(6)	612.4(7)	17.2(6)	2.89(10)
J1919+1341	48.251	0.168	11.66	2020-03-03; 2020-08-07; 2021-05-13; 2021-06-29; 2021-06-29; 2021-07-15; 2022-01-05; 2022-05-29; 2023-01-24; 2023-02-09; 2023-08-09; 2023-08-10; 2023-08-23; 2023-08-26; 2023-11-10; 2024-01-19; 2024-01-30	27000	394(1)	394.0(3)	2.1(1)	4.7(3)
J1920+1110	46.152	−1.199	509.92	2020-05-09	300	186.7(5)	186.7(6)	20.7(3)	3.58(5)
J1920+1340g	48.334	−0.005	1525.92	2023-10-14	900	1053(24)	1053(7)	352(38)	2.0(5)
J1921+1216g	47.214	−0.866	3.00	2023-11-26	900	256.09(2)	256.12(1)	0.97(7)	3.03(5)
J1921+1259g	47.873	−0.583	573.16	2024-02-17	900	357(3)	356.6(16)	38(2)	4.2(3)
J1921+1340g	48.515	−0.297	4603.04	2023-02-14	4590	723(5)	723(5)	160(5)	3.69(10)
J1921+1505g	49.738	0.381	611.90	2020-08-12	900	513(2)	510.6(16)	25(3)	4.3(5)
J1922+1512g	49.933	0.212	2357.21	2022-05-12	900	395(2)	395(3)	78(2)	3.16(7)
J1924+1713	51.988	0.720	758.43	2020-08-08	900	539.0(13)	539(2)	39(2)	3.7(2)
J1928+1245	48.534	−2.290	3.02	2020-09-29	600	179.19(2)	179.192(5)	0.274(8)	3.0(2)
J1928+1923	54.281	1.016	817.40	2020-08-03	300	478.2(5)	476.4(5)	48.2(5)	3.78(4)
J1929+19	54.173	0.568	339.24	2020-11-21	900	524.2(9)	524.5(9)	32.1(3)	2.85(3)
J1946+2433g	60.915	−0.254	8.57	2022-02-02	900	275.2(7)	275.20(9)	4.6(12)	4.8(10)
J1946+2757g	63.847	1.487	742.99	2021-07-07; 2021-07-22	1800	458(3)	450(2)	125(5)	3.1(2)
J1950+2414	61.111	−1.186	4.30	2020-05-13	300	142.04(2)	142.08(2)	0.88(4)	3.2(3)
J1959+3141g	68.424	1.083	514.53	2023-08-25	900	340.6(10)	340.7(2)	15.3(6)	3.8(2)
J2004+3429	71.425	1.571	240.99	2020-04-19	600	354.1(2)	354.1(3)	11.5(1)	4.16(5)
J2005+3411g	71.261	1.229	651.04	2020-08-08; 2021-11-14	1800	483.0(4)	483.0(4)	42.6(10)	3.83(6)
J2015+3404g	72.255	−0.466	4.28	2023-01-06	900	207.98(4)	208.05(4)	1.6(2)	2.8(3)
J2019+3718g	75.379	0.690	505.23	2023-10-17	900	461.6(5)	461.6(7)	24.0(3)	4.28(5)
J2020+3806g	76.145	0.990	525.29	2025-02-28	900	496.8(4)	496.2(3)	10.2(3)	4.9(2)
J2021+3651	75.222	0.111	103.77	2020-03-03; 2020-04-23	900	369.1(5)	369.2(5)	14.5(6)	2.9(2)
J2021+4024g	78.176	2.114	370.56	2020-08-12; 2020-10-13	1800	678.8(10)	678.8(5)	82.1(14)	3.3(3)
J2022+3845g	76.911	1.017	1008.87	2020-08-08; 2020-10-13	1800	483(2)	483(3)	258(8)	4.3(2)
J2022+3910g	77.273	1.237	2036.25	2025-08-13	900	640(4)	641(4)	173(5)	4.7(2)
J2030+3818g	77.449	−0.508	133.72	2021-03-17; 2021-08-11	1800	597.8(7)	596.8(3)	7.8(9)	2.0(5)
J2030+3944g	78.599	0.297	306.19	2020-08-10	900	934.7(10)	934.8(8)	114(4)	3.4(2)
J2032+4055g	79.838	0.646	48.74	2023-10-15	900	372.4(7)	373.7(5)	38(4)	3.1(4)
J2041+3934g	79.745	−1.470	379.97	2024-11-18	900	408(1)	408.2(13)	234(12)	4.8(2)
J2041+4551	84.766	2.334	1160.00	2022-05-01	300	306(1)	306.2(16)	28.4(5)	3.50(2)
J2045+4431g	84.126	0.975	141.82	2024-11-18	900	428(5)	428.5(15)	16.6(9)	3.1(2)
J2046+4236g	82.756	−0.381	523.84	2023-10-15	900	466(10)	466(4)	273(62)	3.7(6)
J2046+4253g	83.016	−0.259	331.15	2022-09-07	900	622.1(8)	622.2(9)	127(4)	3.87(9)
J2052+4421g	84.836	−0.169	375.34	2020-06-07; 2020-08-12; 2021-11-14	2700	543.8(7)	543.8(9)	95(1)	3.46(4)
J2057+4557g	86.597	0.152	225.38	2023-11-23	300	457.0(16)	456.9(3)	48(1)	3.8(1)
J2205+6012	103.686	3.696	2.42	2023-10-18	240	157.55(1)	157.604(6)	0.29(1)	3.5(2)

NOTE— Columns (1) pulsar name, (2) Galactic longitude, (3) Galactic latitude, (4) spin period, (5) FAST observation dates. For some pulsars data from a few dates are added together to get the scattering parameters; (6) the total length of observations in seconds; (7) dispersion measure from the alignment of the front edge at the 1/4 peak level, (8) dispersion measure from the joint fitting, (9) typical pulse-broadening timescale at 1 GHz $\tau_{\rm 1GHz}$, (10) scattering spectral index α. † The scattering parameters of two pulsars are obtained from the model fitting of subband profiles, allowing the frequency evolution of profile components.

ent intrinsic profiles, as done by Lewandowski et al. (2013, 2015a,b).

In the practical fitting calculations, the least-squares method *curve_fit* in the Python package *scipy* is used to obtain an initial estimate of the fitting parameters for each subband profile. Subsequently, the Monte Carlo Markov Chain (MCMC) method *emcee* is implemented to refine the parameters and assess the fitting errors. The best-fit parameters and their errors are determined using the 50th, 16th, and 84th percentiles from the MCMC sampling (see Oswald et al. 2021). The convergence of the MCMC fitting has been visually inspected.

The pulse broadening timescales τ_s measured in this manner of 3 to 5 subbands are obtained, which are listed in Table A1 and then used for a further fitting with a power-law function by the MCMC method to get the scattering spectral index α and also the typical pulse-broadening timescale $\tau_{1\rm GHz}$, as shown in Figure 4.

2.2.2. *Joint fitting subband profiles*

If one can restore the unscattered profiles at multiple frequencies, the DM of a scattered pulsar can be optimized (e.g. Singha et al. 2024). If the length of scattered profiles is larger than the pulsar periods, the baseline of the scattered profile (e.g. Geyer et al. 2017) is hard to measure. We do our best to compensate for the baseline by a freely fitted profile offset or simply skip the data from such subbands or channels. Here, we model the frequency dependence of scattered profiles by assuming the same intrinsic profile in the observing band between 1.0 and 1.5 GHz. Then, we perform the best fit for DM and scattering parameters to the subband profiles.

The intrinsic profile is first modeled from the subband profiles at the highest frequency, as done in the last subsection. The modeled profile of each subband is the convolution of the PBF and the intrinsic profile. Next, when we fit subband profiles together, both ISM effects and intrinsic profiles are optimized simultaneously. The real DM is obtained by aligning the main peaks of the modeled intrinsic profiles across all subbands.

The Monte Carlo Markov Chain (MCMC) method *emcee* is implemented to fit good subband profiles together. We get the model parameters and determine the uncertainties using the 50%, 16%, and 84% percentiles from the MCMC sampling (e.g. Oswald et al. 2021). The convergence of the MCMC has been visually inspected. A new DM is obtained by aligning the main peak of the modeled intrinsic profile components. The above steps are iterated until the DM value is consistent with the previous one within 1σ uncertainty. The final results for pulsar DM and scattering parameters are in the last three columns in Table 1.

2.2.3. *Validation of the fitting results by using the 2-D phase-frequency waterfall plot*

The 2-D phase-frequency waterfall plot with 32 subbands in the FAST observation band of 1.0– 1.5 GHz is used to evaluate the goodness of the fitted scattering parameters. Based on the fitted parameters obtained above, we generate the model subband profiles and then scale them to match the observed subband profiles. For some channels or subbands, we have to adjust the profile baselines for several strongly scattered pulsars. After matching and subtracting, the residual waterfall plot should be random and have no structure, as shown in Fig. 5, if the assumed intrinsic profiles with one, two, or three components and the pulse-broadening functions are reasonable. For almost all cases, the joint fittings have

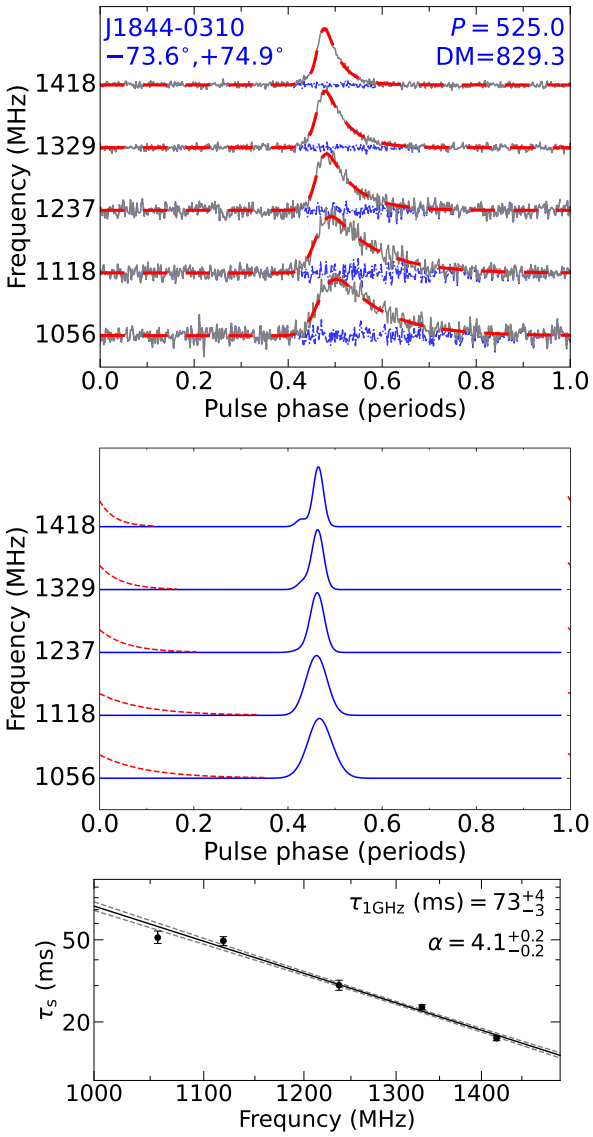


Figure 6: The subband profiles from the FAST observations for PSR J1844−0310 and the results for scattering parameter fittings. *Top panel:* profiles in solid lines and fittings in dashed lines for 5 subbands, together with residuals in short-dashed lines; *Middle panel:* the intrinsic subband profiles obtained from fittings in solid lines together with the PBFs in short-dashed lines; *Bottom panel:* the power-law fitting to the pulse-broadening timescales for the scattering spectral index α.

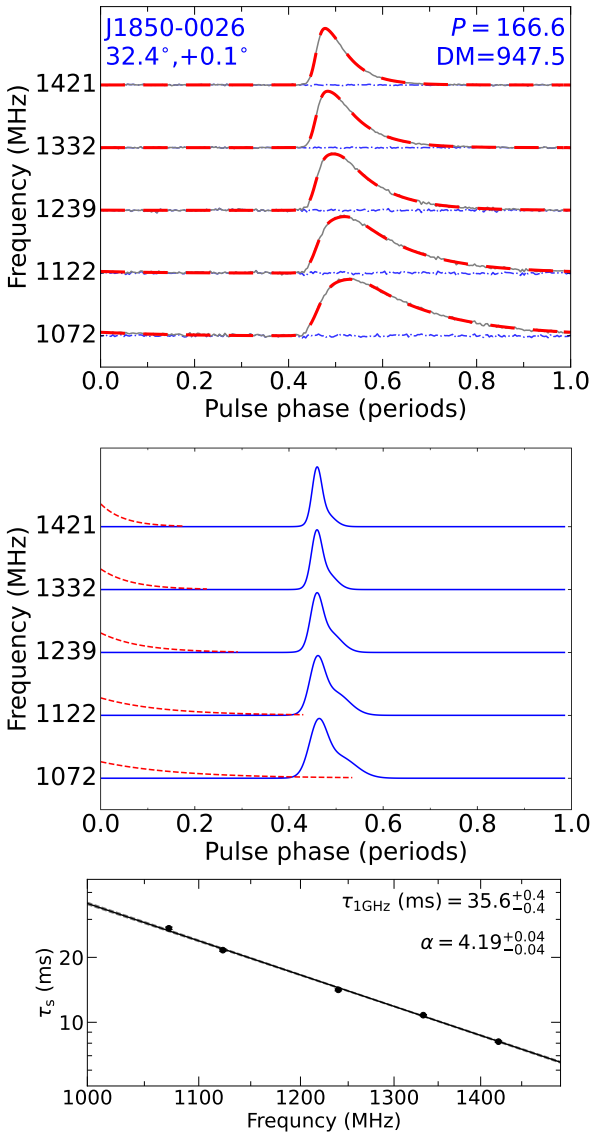


Figure 7: The same as Figure 6 but for PSR J1850−0026.

produced excellent matching to the 2-D phase-frequency waterfall plots, as shown in Figure A1. There are only two exceptional cases in Figure A2; see details below.

2.2.4. *Two exceptional cases*

The two exceptional cases are PSR J1844−0310 and J1850−0026. Through simple joint fitting using the same intrinsic profiles, we obtained the scattering spectral indices 5.7 ± 0.2 for PSR J1844−0310 and 5.76 ± 0.02 for PSR J1850−0026. Both of them show remarkable residuals in the 2-D phase-frequency waterfall plot, and the α value for PSR J1850−0026 is greater than that given by Oswald et al. (2021), as listed in Table 2. The extremely low and seemingly implausible error values observed for the two pulsars are likely due to the fitting process converging on a local optimum. However, when we check the fits to the profiles of individual subbands and the 2-D residual plots, we find a weak frequency-evolving component on the leading edge of PSR J1844−0310 and a weak component on the trailing edge of J1850−0026.

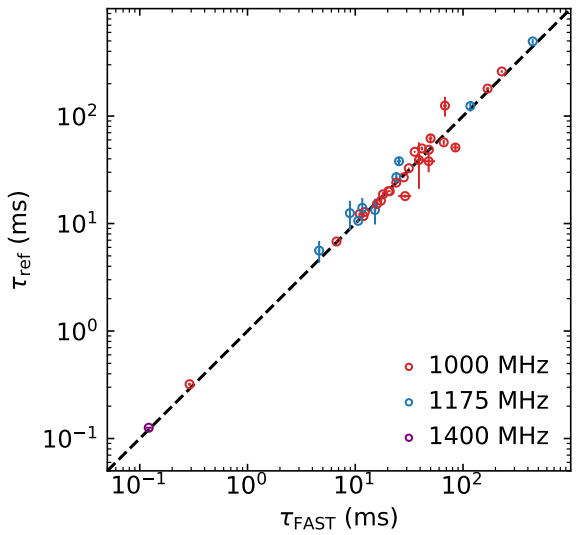


Figure 8: Comparison of pulse-broadening timescales τ measured by FAST and the values in the literature.

As shown in Figure 6, the weak leading component of PSR J1844−0310 becomes more prominent and is mixed with the main component at lower frequencies, making the main component broader at lower frequencies. Using the frequency-evolved intrinsic profiles, we fit the observed subband profiles with the method in Section 2.2.1 and obtain the scattering parameters $\tau_{1\mathrm{GHz}} = 73 \pm 4$ ms and $\alpha = 4.2 \pm 0.2$.

The extra component on the trailing side of PSR J1850−0026 also has frequency evolution and causes more broadening of the observed profiles at the lower frequencies, not only the scattering tails, as shown in Figure 7. As above, using the frequency-evolved intrinsic profiles, we fit the observed subband profiles using the method in Section 2.2.1; we obtain the broadening timescales for all subband profiles and then fit the scattering parameters. Finally, we obtain $\tau_{1\mathrm{GHz}} = 35.6 \pm 0.4$ ms and $\alpha = 4.19 \pm 0.04$.

We therefore understand that, in some cases, only when the reasonable frequency evolution of profile components is considered in model fitting can the scattering parameters be properly estimated.

3. RESULTS AND DISCUSSION

In total, we have measured the scattering parameters for 122 pulsars using data from GPPS and other FAST projects, as indicated by the lengthening tails at lower frequencies in Figure 1 and Figure 5. Plots for all 122 pulsars are presented in Figure A1. The fitted scattering parameters for all 122 pulsars are listed in Table 1, including two DM values obtained by the front-edge alignment and joint fitting, $\tau_{1\mathrm{GHz}}$, and α. It can be observed that the DM values derived from the two approaches are consistent within 3σ of each other.

Table 2: Comparison of pulse-broadening timescale and scattering spectral index from literature and obtained in this paper by FAST observations

PSR Name	Ref	$\nu_{\rm Ref}$ (MHz)	$\tau_{\rm Ref}$ (ms)	$\alpha_{\rm Ref}$	$\tau_{\rm FAST}$ (ms)	$\alpha_{\rm FAST}$
(1)	(2)	(3)	(4)	(5)	(6)	(7)
J1822−1400	[1]	1000	6.81(9)	3.31(8)	6.7(1)	3.27(8)
J1824−1118	[1]	1000	26.9(2)	3.77(2)	28.20(7)	3.890(9)
J1833−0559	[1]	1000	180(6)	3.78(9)	169(6)	3.5(2)
J1835−0643	[1]	1000	110(3)	3.77(7)	110(2)	3.81(6)
J1837−0604	[1]	1000	62(6)	5.01(2)	50(2)	5.4(1)
J1842−0153	[1]	1000	32.7(3)	3.92(5)	31.4(2)	3.38(2)
J1844−0030	[1]	1000	12.3(3)	4.1(2)	11.0(2)	3.19(5)
J1844−0244	[1]	1000	20.0(4)	3.31(9)	20.3(3)	3.48(5)
J1844−0538	[1]	1000	11.73(7)	4.07(3)	11.92(13)	4.06(6)
J1850−0006	[1]	1000	260(7)	4.2(1)	229(3)	3.70(4)
J1850−0026	[1]	1000	46.5(6)	4.946(2)	35.6(4)	4.19(4)
J1852−0127	[1]	1000	57(3)	3.6(1)	66.2(8)	3.89(4)
J1852+0031	[3]	1175	495(25)	-	443.5(13)	3.720(8)
	[3]	1475	225(14)	-	190.3(9)	-
	[2]	2700	36(16)	2.8(10)	-	-
J1853+0505	[3]	1175	124(14)	-	117.0(7)	3.60(2)
	[3]	1475	54(3)	-	51.6(5)	-
J1853+0545	[1]	1000	20.0(3)	3.13(4)	20.9(1)	3.89(2)
	[3]	1175	13.6(20)	-	11.16(7)	-
	[3]	1475	7.1(9)	-	4.61(5)	-
	[3]	2380	1.5(2)	-	-	-
J1855+0205	[4]	1000	16.3(9)	-	17.3(5)	3.4(2)
J1855+0422	[3]	1175	27(3)	-	24.1(6)	4.60(8)
J1856+0245	[4]	1000	18.0(6)	-	29(4)	4.9(6)
J1857+0143	[1]	1000	50(2)	4.0(1)	41.5(9)	3.39(8)
	[5]	1170	24(5)	-	24.4(7)	-
	[5]	2600	0.05(1)	-	-	-
J1857+0210	[3]	1175	13.4(36)	-	15.2(7)	4.6(2)
J1857+0526	[1]	1000	24.0(6)	3.78(7)	24.0(3)	3.82(4)
	[3]	1175	14.5(17)	-	13.0(2)	-
	[3]	1475	6.2(13)	-	5.44(10)	-
J1858+0215	[3]	1175	38(3)	-	25.5(15)	3.1(2)
	[3]	1475	18.4(47)	-	12.6(12)	-
J1859+0601	[1]	1000	125(26)	4.4(7)	68(3)	2.9(2)
J1903+0327	[6]	1400	0.126(1)	-	0.12(3)	4.3(5)
J1908+0839	[3]	1175	5.6(13)	-	4.4(2)	2.75(5)
	[3]	1475	2.6(6)	-	2.23(7)	-
J1908+0909	[3]	1175	4.9(9)	-	5.1(2)	2.36(6)
J1910+0534	[3]	1175	12.5(8)	-	8.9(2)	2.97(5)
J1911+0925	[7]	1000	38(8)	4.3(7)	48(7)	4.0(5)
J1913+1000	[3]	1175	11.1(40)	-	10.6(3)	2.90(6)
J1913+11025	[7]	1000	51(4)	1.6(2)	71(8)	2.6(3)
J1913+1145	[1]	1000	15.2(7)	3.9(2)	15.9(2)	4.19(5)
	[3]	1175	9.2(10)	-	8.1(2)	-
	[3]	1475	4.3(5)	-	3.12(8)	-
J1916+0844	[1]	1000	12.8(1)	4.14(7)	12.27(8)	3.34(3)
	[3]	1175	7.7(10)	-	7.16(6)	-
	[3]	1475	3.6(9)	-	3.35(5)	-
J1919+1314	[4]	1000	18.7(9)	-	18.1(5)	2.89(10)
J1920+1110	[3]	1175	14.0(33)	-	11.6(2)	3.58(5)
	[3]	1475	6.3(21)	-	5.1(2)	-
J1924+1713	[7]	1000	39(18)	4.5(15)	39(2)	3.7(2)
J1928+1923	[1]	1000	48.6(5)	3.94(5)	48.2(5)	3.78(4)
J2205+6012	[8]	1000	0.32(1)	3.71(6)	0.29(1)	3.5(2)

NOTE— Columns (1) pulsar name, (2) reference for public scattering parameters, (3) central frequency of the pulse broadening timescale of the reference, (4) pulse-broadening timescale at the given frequency, (5) public scattering spectral index, (6) pulse-broadening timescale at the reference frequency interpolated by scattering parameters in this paper, (9) scattering spectral index measured by FAST. The references are marked as: [1] Oswald et al. (2021); [2] Löhmer et al. (2001); [3] Bhat et al. (2004); [4] Nice et al. (2013); [5] Lewandowski et al. (2013); [6] Champion et al. (2008); [7] Parent et al. (2022); [8] Desvignes et al. (2022).

3.1. *Pulsar scattering parameters in literature and comparison with FAST measurements*

To investigate the DM and direction dependence of scattering effects and to compare FAST-measured scattering parameters with literature values, we need to collect all previously published measurements of scattering parameters. We noticed that He & Shi (2024) collected scattering times for 473 pulsars from 54 papers. In our full collection, 497 pulsars have the pulse-broadening timescale measured in the reference. We only use measurements of $\tau_{\rm s}$ with a relative uncertainty better than 10 percent. Most of them are reliable measurements from wide-band observations (Oswald et al. 2021) with prominent scattering features in profiles.

Many pulsars have their scattering parameters measured by Bhat et al. (2004); Nice et al. (2013); Zakharenko et al. (2013); Lewandowski et al. (2013, 2015a,b); Geyer et al. (2017); Krishnakumar et al. (2015, 2017, 2019); Oswald et al. (2021); Kravtsov et al. (2022) where observations were made at multiple frequencies. Some pulsars at specific Galactic positions also show scattering profiles (Johnston et al. 2006; Deneva et al. 2009; Bansal et al. 2019; Kirsten et al. 2019; Surnis et al. 2019; Gautam et al. 2022; Kravtsov et al. 2022; Parent et al. 2022; Sengar et al. 2023). In addition, scattering parameters have been observed for some specific pulsars, such as PSRs J0026+6320 and J2217+5733 (Surnis et al. 2019), J0534+2200 (Crab) (Kuz'min et al. 2002, 2007; Bhat et al. 2007, 2008; Oronsaye et al. 2015; Ellingson et al. 2013; Eftekhari et al. 2016; Meyers et al. 2017), J0540-6919 via giant pulse observations (Johnston & Romani 2003; Geyer et al. 2021), J0835-4510 (Vela) (Ables et al. 1970), J1208-5936 (Bernadich et al. 2023), J1227-6208 (Bernadich et al. 2024), J1410-6132 (O'Brien et al. 2008), J1550-5418 (Camilo et al. 2007), J1638-4713 (Lazarević et al. 2024), J1717-4054 (Kerr et al. 2014), J1744-2946 (Lower et al. 2024), J1745-2900 (Spitler et al. 2014; Pennucci et al. 2015), J1746-2829 (Wongphechauxsorn et al. 2023), J1747-2809 towards the Galactic Center (Camilo et al. 2009), J1751-2737 at the Galactic Center (Bhakta et al. 2017), J1752-2806 (Xue et al. 2019), J1813-1749 near the Galactic Center (Camilo et al. 2021), J1823-3021A from giant-pulse observations (Ho et al. 2025), J1841-0050 (Camilo et al. 2012; Wang et al. 2020), J1939+2134 (Cordes et al. 1990), J1949+3426 (Aloisi et al. 2019), J1959+2048 from giant-burst observations (Main et al. 2017), J2113+4644 (Smirnova & Shishov 2010), and J2205+6012 (Desvignes et al. 2022).

After collecting all the data and discarding some uncertain values, we get the scattering parameters of 243 pulsars.

Among the 158 pulsars we measured, the scattering parameters for 121 pulsars are determined for the first time, including 71 newly discovered pulsars by the FAST GPPS survey. In contrast, the scattering parameters of the other 37 pulsars have been measured previously in the literature, and they are also listed in Table 2.

Based on our measurements of τ_s in different subbands in Table A1 and the scattering spectral index α in Table 1, we interpolate the pulse-broadening timescale $\tau_{\rm FAST}$ at the frequency specified in the literature where $\tau_{\rm ref}$ was obtained. Then we compare $\tau_{\rm FAST}$ with $\tau_{\rm ref}$, and find that they are in good agreement with each other, as shown in Figure 8.

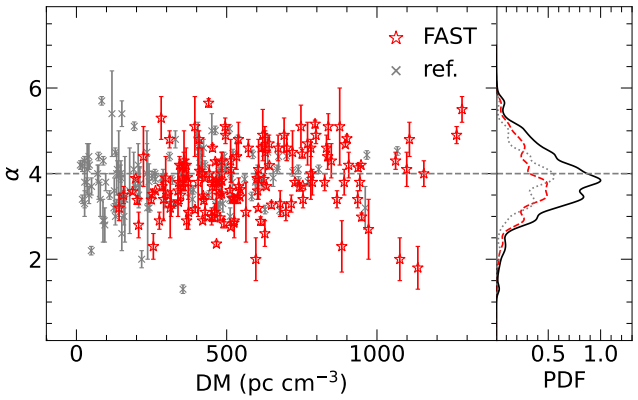


Figure 9: Distribution of scattering spectral indexes α for pulsars measured by FAST and pulsars in the literature, peaked around $\alpha = 4.0$. The probability distribution function (PDF) in the right subpanel is composed by summing the Gaussian functions defined by the α and uncertainty.

Among 158 pulsars, we find that the scattering spectral indexes for 24 pulsars (including 4 pulsars with the error bar of α greater than 0.5) have been determined previously, as listed in Table 2. The α value of PSR J1913+11025 obtained by Parent et al. (2022) is 1.6 ± 0.2, which is very low compared with the others. We noticed a possible weak component on the trailing tail in the profile of Parent et al. (2022) and in our subband profiles by the FAST. Then, we fit the profiles with an intrinsic profile with two Gaussian components and get $\alpha = 2.5 \pm 0.2$.

As mentioned in the introduction, the scattering spectral indices can differ across different parts of the turbulent medium; for example, $\alpha = 4.0$ for the Gaussian distribution of fluctuations, or $\alpha = 4.4$ for a general medium with a Kolmogorov spectrum (Cordes & Lazio 1991). One can find that the α values in Figure 9 have a wide distribution around 4.0, and are consistent with the results given by e.g. Lewandowski et al. (2015b) and Oswald et al. (2021). Physically, several reasons can cause the deviations of the α values: (1) the inner cutoff of the wavenumber spectrum, reducing α as low as 2 when the scattering angle is less than a critical cross-over angle (Cordes & Lazio 2003; Lewandowski et al. 2015a); (2) a low α down to 2.6 in the highly supersonic turbulence with a short-wave-dominated density spectrum (Xu & Zhang 2017); (3) a non-Kolmogorov form for the density spectrum (Bhat et al. 2004); (4) a finite size of screens such as filamentary structures or clumps (Cordes & Lazio 2001); (5) the anisotropic scattering media (Brisken et al. 2010; Geyer & Karastergiou 2016).

3.2. *Dependence of $\tau_{\rm s}$ with DM*

For analyzing the DM and direction dependence of the scattering effect, all measured pulse-broadening timescales

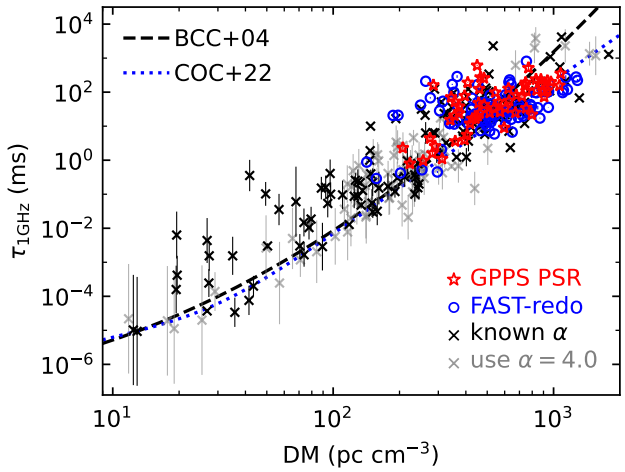


Figure 10: The distribution of the pulse-broadening timescale τ_s at 1 GHz versus pulsar DM. The values of newly discovered pulsars in the GPPS survey and the known pulsars re-detected by the FAST are specially marked by stars and circles. The other values are extrapolated from measurements at other frequencies, either using the previously estimated α or by assuming $\alpha = 4.0$. Two empirical relations given by Bhat et al. (2004) and Cordes et al. (2022) are outlined by a dashed line and a dotted line.

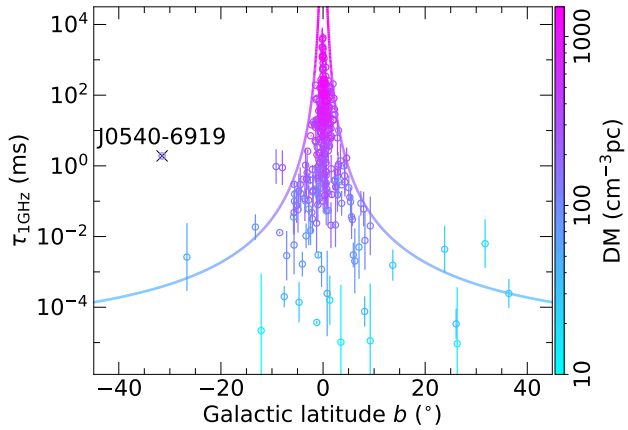


Figure 11: Pulse-broadening timescale $\tau_{1\mathrm{GHz}}$ of pulsars at various Galactic latitudes, together with the upper limit curve calculated by the DM upper limit.

τ_s are scaled to $\tau_{1\mathrm{GHz}}$ by using the estimated scattering spectral index α. If no observed α is available, we take $\alpha = 4.0$ for scaling τ_s. The accuracy of such extrapolated pulse-broadening timescales rests on the uncertainty of α (Slee et al. 1980), and we take $\Delta\alpha = 0.6$, which is the standard deviation of α given by Oswald et al. (2021).

The pulse-broadening timescales $\tau_{1\mathrm{GHz}}$ are related to the dispersion measure by an empirical formula expressed in Eq.(3) (Bhat et al. 2004; Cordes et al. 2022), as shown in Figure 10. Our new FAST measurements contribute new data at the high DMs and are consistent with the trend.

3.3. *Dependence of τ_s on the spatial distribution of the interstellar medium*

The scattering effect is caused by ionized gas clouds between a pulsar and us. Therefore the pulse-broadening timescale $\tau_{1\mathrm{GHz}}$ and the scattering spectral index α depend on the foreground clouds (e.g. Lewandowski et al. 2015a). Some low-DM pulsars show varying scattering effects (Bansal et al. 2019) because they are behind HII regions or supernova remnants (Krishnakumar et al. 2019). Here we investigate the dependence of τ_s on the spatial distribution of the interstellar medium.

First of all, the scattering effect varies with the Galactic latitude (Cordes et al. 1984; Ocker et al. 2021; Koryukova et al. 2022; He & Shi 2024). The upper limit of the pulse-broadening timescale, as shown in Figure 11, can be derived by combining the τ_s-DM relation (Equation 3) with the upper limit of the Galactic DM of $\mathrm{DM_{max}} = (23.5 \pm 2.5)\ \mathrm{pc\ cm^{-3}}/\sin(b)$ (Ocker et al. 2020). Notably, the large pulse-broadening timescale of PSR J0540−6919 should be attributed to the medium in the Large Magellanic Cloud (Cordes et al. 2016).

Secondly, one may find that pulsars behind different spiral arms or HII regions show different dependence of τ_s on DM. By using the scattering parameters measured in this paper and compiled data from the literature, we aim to explore the dependence of τ_s on different density fluctuations in different spiral arms (Cordes & Rickett 1998; Ocker et al. 2022)

$$\tilde{F} = (\tau_{1\mathrm{GHz}}/\,0.48\ \mathrm{ms})(DM/100\ \mathrm{cm^{-3}pc})^{-2} \qquad (6)$$

in different Galactic disk regions as divided in Figure 12. Here $\tilde{F}$ is a fluctuation parameter, characterizing density fluctuations in turbulence (Cordes et al. 2016; Ocker et al. 2021). Our approach is similar to the work of Alurkar et al. (1986) and Pynzar' & Shishov (2008), and to the investigations of the Sun-local region, the inner disk, and the outer disk conducted by Krishnakumar et al. (2015) and He & Shi (2024). The Galactic disk region is divided into different sections based on the Galactic longitudes (e.g. Pushkarev et al. 2026). Specifically, regions dominated by the Perseus arm, the Sagittarius-Carina (Sag-Car) arm, and the Scutum-Centaurus (Scu-Cen) arm are distinct, with each arm corresponding to specific ranges of Galactic longitude.

The pulse-broadening timescales $\tau_{1\mathrm{GHz}}$ and fluctuation parameter $\tilde{F}$ for pulsars in these radial sectors are plotted in Figure 13(a1) to (c1) and (a2) to (c2). The fluctuation parameter $\tilde{F}$ of different arm regions is shown in Figure 13(a2) to (c2). The figure clearly shows that the data are clustered across different DM values and $\tilde{F}$ values, implying that the interstellar medium in different spiral arms has distinct fluctuation properties. Their probability density functions (PDFs) of the fluctuation parameter $\tilde{F}$ for scattered pulsars can be expressed as multiple Gaussian functions, for example, for these pulsars in the highlighted regions corresponding to spiral arms at different distances. In the Perseus Arm region, there are two groups of pulsars; in the Sagittarius-Carina region, there are also two groups of pulsars with dif-

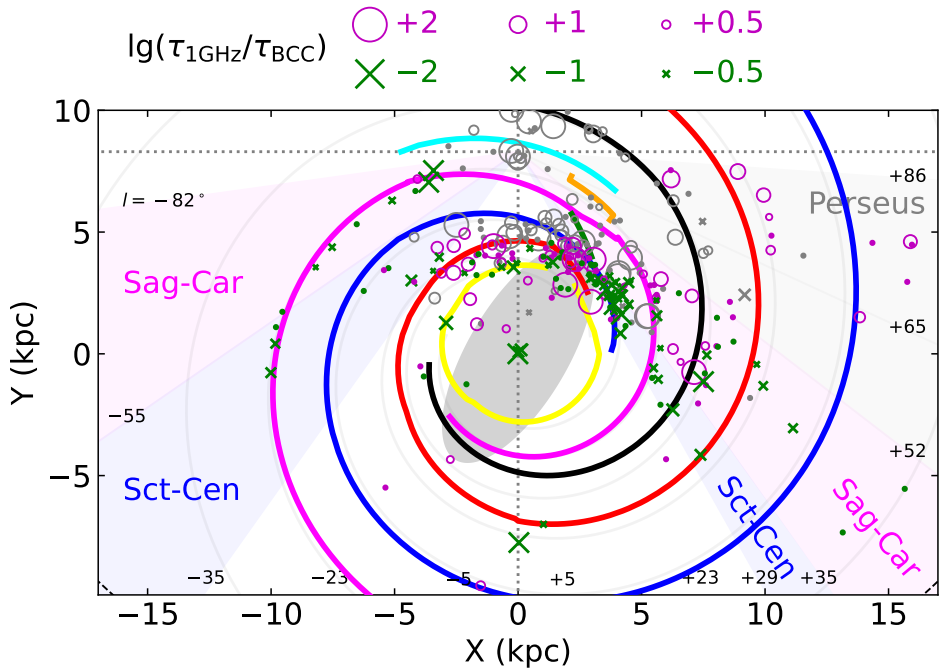


Figure 12: Distribution of scattered pulsars with $|b| < 5°$ in various spiral arm regions outlined by Hou & Han (2014) and Reid et al. (2019). Crosses and circles indicate the relative $\tau_{1\rm GHz}$ deviation from the empirical prediction given by Equation 3. Pulsars with DM < 300 pc cm^{-3} are plotted in gray. The Galactic disk is divided into and labeled by the dominant spiral arms, namely the Perseus arm, the Sagittarius-Carina (Sag-Car) arm, and the Scutum-Centaurus (Scu-Cen) arm.

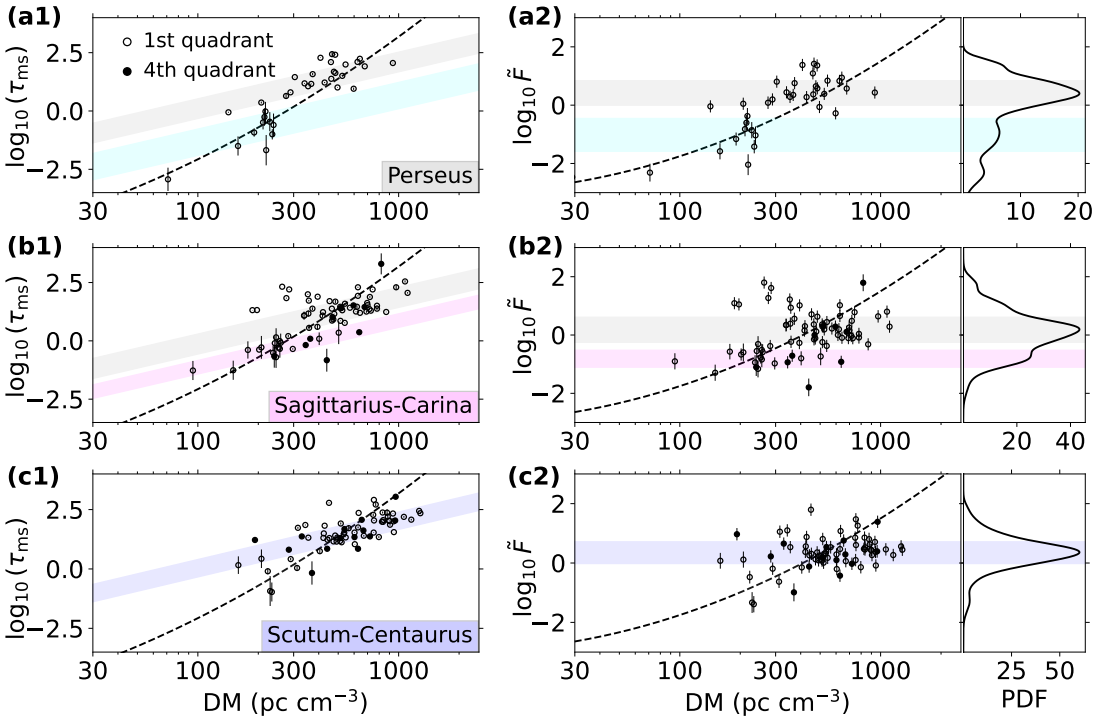


Figure 13: The pulse-broadening timescales $\tau_{1\rm GHz}$ and the fluctuation parameter $\tilde{F}$ for scattered pulsars in different regions dominated by different spiral arms as marked in Figure 12. The dashed line is drawn according to the empirical $\tau_{\rm s}$-DM formula in Equation 3. The probability distribution function (PDF) of $\tilde{F}$ for pulsars in the highlighted area is expressed with the Gaussian functions in the left sub-panels. The open and filled circles label pulsars in the first and fourth Galactic quadrants.

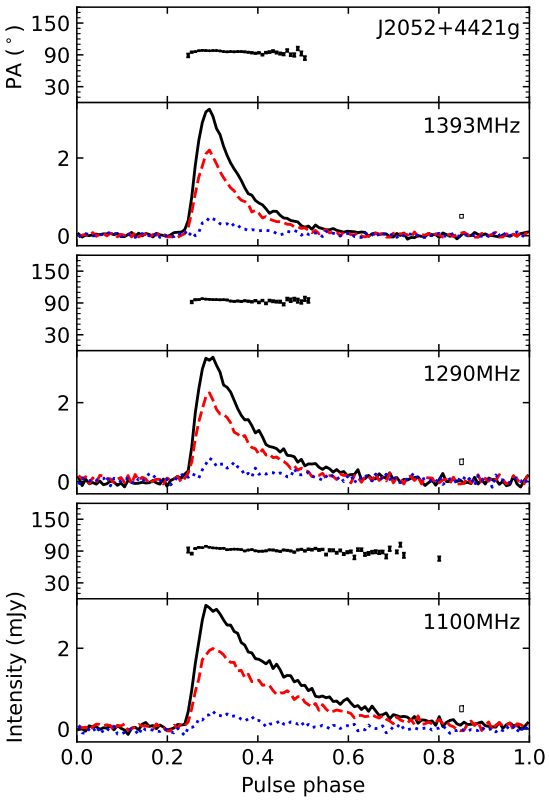


Figure 14: Polarization profiles of PSR J2052+4421g at three subbands of FAST observations. For each subband, the total intensity profile is drawn by the solid line, the linear polarization profile by the dashed line, and the circular polarization profile by the dotted line in the lower sub-panel. The box indicates the phase bin size and the $\pm 1\sigma$ range. The polarization position angles (PAs) with error bars are shown in the top sub-panel. The polarization profiles of another 40 well-calibrated pulsars are presented in Fig. A4.

ferent DMs and fluctuation parameters; in contrast, in the Scutum-Centaurus region, only one pulsar group shows the scattering effect.

The grouping of pulsars with high fluctuations and high DMs implies that they are behind a given identifiable spiral arm. Therefore, the distances of these pulsars can be constrained as proposed in Frail & Clifton (1989); Cordes & Rickett (1998); Lazio et al. (2004). For example, the two fluctuation groups in the Perseus arm region (see Figure 13 a1-a2) should correspond to the pulsars in or behind the local arm or the pulsars in or behind the Perseus arm.

3.4. *Polarization profiles*

Using the DMs from the joint fitting and calibrating the FAST data, we can obtain subband polarization profiles for pulsars with strong scattering features. Polarimetric calibration of the pulse profiles has been conducted by using PSRCHIVE (van Straten 2004) following the detailed procedures given in Wang et al. (2023) (van Straten 2004). The Faraday rotation measure (RM) is obtained from the *RMFIT* in the PSRCHIVE software routine. After Faraday rotation is fitted and corrected for the channel data, we obtain the final observed RMs and polarization profiles.

Figure 14 is one example, showing the polarization profiles of PSR J2052+4421g at three subbands of FAST observations. The profiles are more extended at lower frequencies. Polarization angle curves flatten in the scattered profile tails, as discussed by Li & Han (2003). The subband polarization profiles for another 40 pulsars observed by FAST are shown in Figure A4, and their polarization parameters are listed in Table A2.

4. CONCLUSIONS

We present the pulse-broadening timescales and scattering spectral indices for 158 pulsars derived from FAST observations at the L-band (1.0–1.5 GHz). The measurements of 121 pulsars are obtained for the first time. For 37 pulsars with the scattering parameters reported in the literature, our measurements are generally consistent with previously reported values, though there are a few exceptions.

We find that aligning the front edge of the subband profiles at the half or quarter of the profile peak can yield better DM values for most pulsars than those obtainable using *PDMP*. However, the best DM value can be determined by aligning the main peak of the modeled intrinsic profiles obtained from joint fitting the scattered subband profiles.

We find that in regions with spiral arms, the pulsars can be grouped by their DM values and relative fluctuations, which indicate density irregularities in these regions. On the other hand, the grouping of pulsars can probably be a rough indication of pulsar locations.

From the FAST observations, polarized profiles have been obtained for 82 pulsars across three subbands, consistently showing flattened polarization-angle curves in the scattered-profile tails, as suggested by Li & Han (2003).

ACKNOWLEDGEMENTS

We thank the referee, Prof. Ramesh Bhat, for very careful reading and helpful suggestions. The authors were supported by the National Key R&D Program of China No. 2025YFA1614003, National Natural Science Foundation of China (NSFC), grant numbers 12588202, 12041303, and 12225304, the Chinese Academy of Sciences via project JZHKYPT-2021-06. the National SKA Program of China (2020SKA0120100), the National SKA Program of China (grant No. 2022SKA0120103) and the Chinese Academy of Sciences via the project JZHKYPT-2021-06. FAST is a Chinese national mega-science facility built and operated by the National Astronomical Observatories of the Chinese Academy of Sciences. We all appreciate the excellent performance of FAST and the operation team.

APPENDIX

This appendix presents big databases, including two long tables and figures.

The FAST observations were carried out in the band of 1.0-1.5 GHz, with various RFI in different frequency channels for

different pulsars at different times. Considering these various RFI situations, we measured the pulse-broadening timescales at these sub-bands, and published them directly in Table A1.

Figure A1 presents the scattering profiles in 3-5 subbands for pulsars which have been well-fitted in the joint model-fitting to subband profiles, except for PSR J1844-0310 and J1850-0026, which probably have frequency-evolution for intrinsic profile components and are presented in Figure A2 and A3.

The polarized subband profiles for 82 scattered pulsars are presented in Figure A4. The polarization parameters are given in Table A2.

REFERENCES

Ables, J. G., Komesaroff, M. M., & Hamilton, P. A. 1970, Astrophys. Lett., 6, 147

Aloisi, R. J., Cruz, A., Daniels, L., et al. 2019, ApJ, 875, 19, doi: 10.3847/1538-4357/ab0d21

Alurkar, S. K., Bobra, A. D., & Slee, O. B. 1986, Australian Journal of Physics, 39, 433, doi: 10.1071/PH860433

Andersen, B. C., Fonseca, E., McKee, J. W., et al. 2023, ApJ, 943, 57, doi: 10.3847/1538-4357/aca485

Bansal, K., Taylor, G. B., Stovall, K., & Dowell, J. 2019, ApJ, 875, 146, doi: 10.3847/1538-4357/ab0d8f

Bathula, A., Krishnakumar, M. A., & Jena, S. 2026, PASA, 43, e032, doi: 10.1017/pasa.2026.10160

Bernadich, M. C. i., Balakrishnan, V., Barr, E., et al. 2023, arXiv e-prints, arXiv:2308.16802, doi: 10.48550/arXiv.2308.16802

Bernadich, M. C. i., Venkatraman Krishnan, V., Champion, D. J., et al. 2024, arXiv e-prints, arXiv:2407.13593, doi: 10.48550/arXiv.2407.13593

Bhakta, D., Deneva, J. S., Frail, D. A., et al. 2017, MNRAS, 468, 2526, doi: 10.1093/mnras/stx656

Bhat, N. D. R., Cordes, J. M., Camilo, F., Nice, D. J., & Lorimer, D. R. 2004, ApJ, 605, 759, doi: 10.1086/382680

Bhat, N. D. R., Cordes, J. M., & Chatterjee, S. 2003, ApJ, 584, 782, doi: 10.1086/345775

Bhat, N. D. R., Tingay, S. J., & Knight, H. S. 2008, ApJ, 676, 1200, doi: 10.1086/528735

Bhat, N. D. R., Wayth, R. B., Knight, H. S., et al. 2007, ApJ, 665, 618, doi: 10.1086/519444

Bhattacharya, D., Wijers, R. A. M. J., Hartman, J. W., & Verbunt, F. 1992, A&A, 254, 198

Brisken, W. F., Macquart, J. P., Gao, J. J., et al. 2010, ApJ, 708, 232, doi: 10.1088/0004-637X/708/1/232

Camilo, F., Ransom, S. M., Chatterjee, S., Johnston, S., & Demorest, P. 2012, ApJ, 746, 63, doi: 10.1088/0004-637X/746/1/63

Camilo, F., Ransom, S. M., Gaensler, B. M., & Lorimer, D. R. 2009, ApJL, 700, L34, doi: 10.1088/0004-637X/700/1/L34

Camilo, F., Ransom, S. M., Halpern, J. P., & Reynolds, J. 2007, ApJL, 666, L93, doi: 10.1086/521826

Camilo, F., Ransom, S. M., Halpern, J. P., & Roshi, D. A. 2021, ApJ, 917, 67, doi: 10.3847/1538-4357/ac0720

Champion, D. J., Ransom, S. M., Lazarus, P., et al. 2008, Science, 320, 1309, doi: 10.1126/science.1157580

Chen, X., Han, J. L., Su, W. Q., Yang, Z. L., & Zhou, D. J. 2023a, Research in Astronomy and Astrophysics, 23, 104004, doi: 10.1088/1674-4527/acd52b

Chen, X., Yan, Y., Han, J. L., et al. 2023b, Nature Astronomy, 7, 1235, doi: 10.1038/s41550-023-02056-z

Cordes, J. M., Ananthakrishnan, S., & Dennison, B. 1984, Nature, 309, 689, doi: 10.1038/309689a0

Cordes, J. M., & Lazio, T. J. 1991, ApJ, 376, 123, doi: 10.1086/170261

Cordes, J. M., & Lazio, T. J. W. 1997, ApJ, 475, 557, doi: 10.1086/303569

—. 2001, ApJ, 549, 997, doi: 10.1086/319442

Cordes, J. M., & Lazio, T. J. W. 2002, arXiv e-prints, astro. https://arxiv.org/abs/astro-ph/0207156

—. 2003, arXiv e-prints, astro. https://arxiv.org/abs/astro-ph/0301598

Cordes, J. M., Ocker, S. K., & Chatterjee, S. 2022, ApJ, 931, 88, doi: 10.3847/1538-4357/ac6873

Cordes, J. M., & Rickett, B. J. 1998, ApJ, 507, 846, doi: 10.1086/306358

Cordes, J. M., Weisberg, J. M., & Boriakoff, V. 1985, ApJ, 288, 221, doi: 10.1086/162784

Cordes, J. M., Wharton, R. S., Spitler, L. G., Chatterjee, S., & Wasserman, I. 2016, arXiv e-prints, arXiv:1605.05890. https://arxiv.org/abs/1605.05890

Cordes, J. M., Wolszczan, A., Dewey, R. J., Blaskiewicz, M., & Stinebring, D. R. 1990, ApJ, 349, 245, doi: 10.1086/168310

Cronyn, W. M. 1970, Science, 168, 1453, doi: 10.1126/science.168.3938.1453

Demorest, P. B. 2011, MNRAS, 416, 2821, doi: 10.1111/j.1365-2966.2011.19230.x

Deneva, J. S., Cordes, J. M., & Lazio, T. J. W. 2009, ApJL, 702, L177, doi: 10.1088/0004-637X/702/2/L177

Desvignes, G., Cognard, I., Smith, D. A., et al. 2022, A&A, 667, A79, doi: 10.1051/0004-6361/202244171

Dexter, J., Deller, A., Bower, G. C., et al. 2017, MNRAS, 471, 3563, doi: 10.1093/mnras/stx1777

Eftekhari, T., Stovall, K., Dowell, J., Schinzel, F. K., & Taylor, G. B. 2016, ApJ, 829, 62, doi: 10.3847/0004-637X/829/2/62

Ellingson, S. W., Clarke, T. E., Craig, J., et al. 2013, ApJ, 768, 136, doi: 10.1088/0004-637X/768/2/136

Table A 1: Pulse-broadening timescales τ_s measured for subband profiles from FAST observations. The FAST observation band is divided into 3 – 5 subbands according to the RFI situation so that the central frequencies of subbands differ from pulsar to pulsar and are given in the table. This table is available in its entirety in the online supplementary material at ScienceDB https://doi.org/10.57760/sciencedb.j00167.0002b.

PSR Name	τ_s@ν_1 (ms@MHz)	τ_s@ν_2 (ms@MHz)	τ_s@ν_3 (ms@MHz)	τ_s@ν_4 (ms@MHz)	τ_s@ν_5 (ms@MHz)
J0248+6021	23.45±0.01@1096	17.87±0.01@1178	11.34±0.00@1320	9.12±0.00@1404	
J1822−1252	228±19@1106	107±6@1269	72±9@1380		
J1822−1400	4.94±0.08@1111	3.2±0.1@1245	2.0±0.1@1402		
J1823−11	659±472@1107	103^{+32}_{-20}@1269	65±7@1380		
J1823−1312g	155^{+69}_{-36}@1107	54±6@1263	52±4@1380		
J1823−1344g	84^{+28}_{-19}@1095	25±4@1351	23±4@1404		
J1823−1347	25.2±0.6@1095	19.8±0.7@1184	14.2±0.6@1318	12.1±0.6@1404	
J1824−1118	20.90±0.06@1076	14.30±0.04@1186	9.48±0.02@1321	7.47±0.03@1417	
J1829−1132g	22±2@1111	14±1@1229	10±0@1358		
J1831−1127g	30±2@1102	25±2@1273	15±1@1381		
J1833−0204g	0.5±0.1@1105	0.4±0.1@1259	0.2±0.1@1399		
J1833−0556	139±4@1078	102±3@1183	73±2@1322	56±3@1420	
J1833−0559	160±10@1061	126±10@1125	61±1@1351	47±2@1433	

... to be continued.

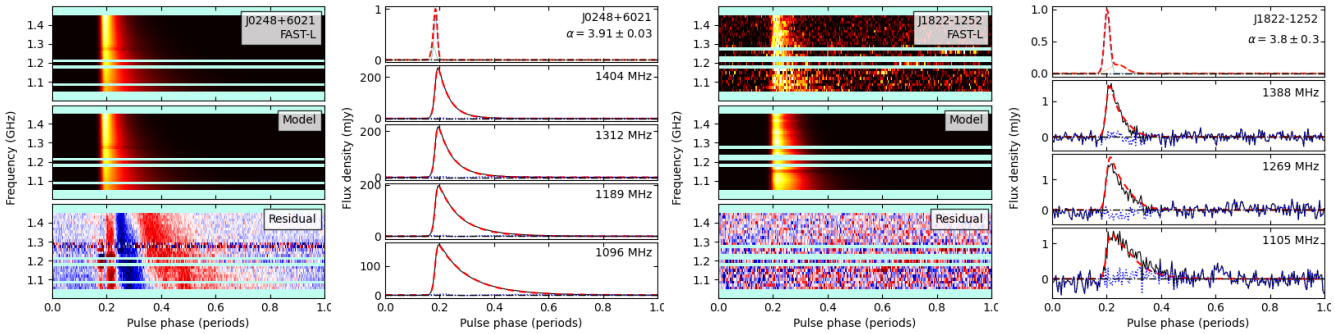


Figure A 1: The observed and modeled scattering profiles for 156 pulsars. Comparing the phase-time waterfall 2D intensity plot for the 32 channels in the FAST observation band (left top) with the modeled scattered profiles (left middle), one can get the residual plot (left bottom). The intrinsic profiles and the modeled subband profiles are given on the right. This figure is available in its entirety in the online supplementary material at ScienceDB https://doi.org/10.57760/sciencedb.j00167.0002b.

Fonseca, E., Pleunis, Z., Breitman, D., et al. 2024, ApJS, 271, 49, doi: 10.3847/1538-4365/ad27d6

Frail, D. A., & Clifton, T. R. 1989, ApJ, 336, 854, doi: 10.1086/167056

Gautam, T., Ridolfi, A., Freire, P. C. C., et al. 2022, A&A, 664, A54, doi: 10.1051/0004-6361/202243062

Geyer, M., & Karastergiou, A. 2016, MNRAS, 462, 2587, doi: 10.1093/mnras/stw1724

Geyer, M., Karastergiou, A., Kondratiev, V. I., et al. 2017, MNRAS, 470, 2659, doi: 10.1093/mnras/stx1151

Geyer, M., Serylak, M., Abbate, F., et al. 2021, MNRAS, 505, 4468, doi: 10.1093/mnras/stab1501

Han, J. L., Wang, C., Wang, P. F., et al. 2021, Research in Astronomy and Astrophysics, 21, 107, doi: 10.1088/1674-4527/21/5/107

Han, J. L., Zhou, D. J., Wang, C., et al. 2024, Research in Astronomy and Astrophysics, submitted

He, Q., & Shi, X. 2024, MNRAS, 527, 5183, doi: 10.1093/mnras/stad3561

He, Q., Shi, X., & Li, G. 2025, arXiv e-prints, arXiv:2502.09158. https://arxiv.org/abs/2502.09158

Hessels, J. W. T., Spitler, L. G., Seymour, A. D., et al. 2019, ApJL, 876, L23, doi: 10.3847/2041-8213/ab13ae

Ho, S. C. C., Bailes, M., Flynn, C., & Abbate, F. 2025, arXiv e-prints, arXiv:2506.14887. https://arxiv.org/abs/2506.14887

Hotan, A. W., van Straten, W., & Manchester, R. N. 2004, PASA, 21, 302, doi: 10.1071/AS04022

Hou, L. G., & Han, J. L. 2014, A&A, 569, A125, doi: 10.1051/0004-6361/201424039

Jiang, P., Tang, N.-Y., Hou, L.-G., et al. 2020, Research in Astronomy and Astrophysics, 20, 064, doi: 10.1088/1674-4527/20/5/64

Jing, W. C., Han, J. L., Hong, T., et al. 2023, MNRAS, 523, 4949, doi: 10.1093/mnras/stad1782

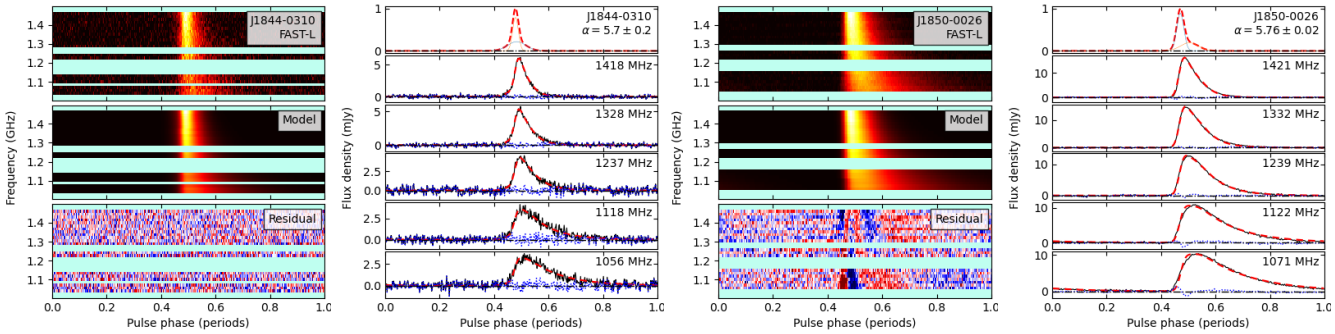


Figure A 2: The same as Figure 1 but for two unusual pulsars, PSR J1844-0310 and J1850-0026, which have to include the frequency-evolution for intrinsic profile components for the modeling, otherwise remarkable residuals will be left.

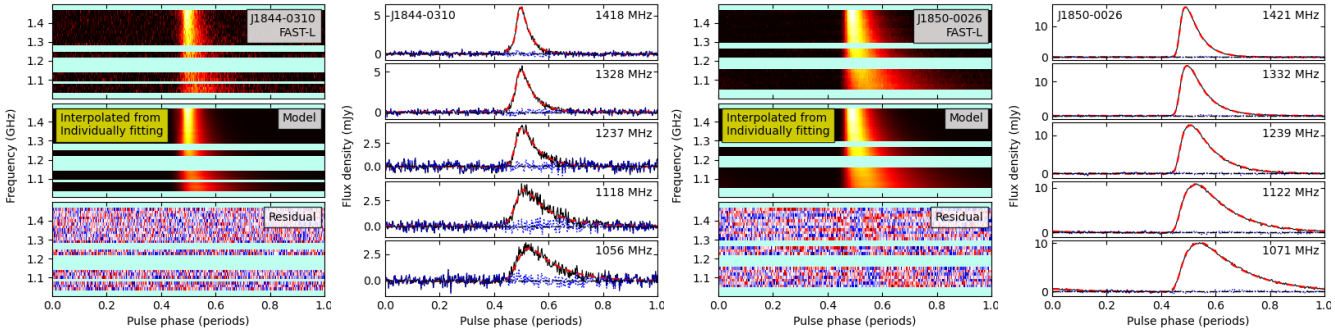


Figure A 3: The validation plot of two unusual pulsars, PSR J1844-0310 and J1850-0026, with the interpolated intrinsic profile from the individual fitting. Their residuals reach the noise level.

Table A 2: Polarization parameters of subband profiles and the rotation measures for 82 scattered pulsars observed by FAST. This table is available in its entirety in the online supplementary material at ScienceDB https://doi.org/10.57760/sciencedb.j00167.0002b.

PSR Name	FAST Obs. Date yyyy-mm-dd	RM ($\mathrm{rad/m^2}$)	f (MHz)	I (μJy)	L/I (%)	V/I (%)	$\lvert V\rvert/I$ (%)
J0248+6021	2023-08-14	-149.990 ± 0.005	1110	22263 ± 1113	69.4 ± 3.0	0.3 ± 3.0	0.3 ± 3.0
			1265	17345 ± 867	71.9 ± 3.0	2.2 ± 3.0	2.2 ± 3.0
			1384	15012 ± 750	71.6 ± 3.0	1.6 ± 3.0	1.7 ± 3.0
J1822-1400	2026-04-24	$+895.8 \pm 0.9$	1109	717 ± 45	19.9 ± 3.1	-5.7 ± 3.1	5.1 ± 3.1
			1255	471 ± 40	19.4 ± 3.2	-7.5 ± 3.1	5.6 ± 3.1
			1411	343 ± 33	18.3 ± 3.2	-8.0 ± 3.1	7.5 ± 3.1
J1824-1118	2025-08-18	$+184.9 \pm 0.2$	1100	2527 ± 126	22.0 ± 3.0	0.7 ± 3.0	4.6 ± 3.0
			1259	1712 ± 86	19.2 ± 3.0	-1.4 ± 3.0	5.7 ± 3.0
			1388	1387 ± 69	17.6 ± 3.0	-1.6 ± 3.0	7.8 ± 3.0

Johnston, S., Kramer, M., Lorimer, D. R., et al. 2006, MNRAS, 373, L6, doi: 10.1111/j.1745-3933.2006.00232.x

Johnston, S., & Romani, R. W. 2003, ApJL, 590, L95, doi: 10.1086/376826

Karastergiou, A. 2009, MNRAS, 392, L60, doi: 10.1111/j.1745-3933.2008.00585.x

Kerr, M., Hobbs, G., Shannon, R. M., et al. 2014, MNRAS, 445, 320, doi: 10.1093/mnras/stu1716

Kirsten, F., Bhat, N. D. R., Meyers, B. W., et al. 2019, ApJ, 874, 179, doi: 10.3847/1538-4357/ab0c05

Komesaroff, M. M., Hamilton, P. A., & Ables, J. G. 1972, Australian Journal of Physics, 25, 759, doi: 10.1071/PH720759

Koryukova, T. A., Pushkarev, A. B., Plavin, A. V., & Kovalev, Y. Y. 2022, MNRAS, 515, 1736, doi: 10.1093/mnras/stac1898

Kramer, M. 1994, A&AS, 107, 527

Kravtsov, I. P., Zakharenko, V. V., Ulyanov, O. M., et al. 2022, MNRAS, 512, 4324, doi: 10.1093/mnras/stab3369

Krishnakumar, M. A., Joshi, B. C., & Manoharan, P. K. 2017, ApJ, 846, 104, doi: 10.3847/1538-4357/aa7af2

Krishnakumar, M. A., Maan, Y., Joshi, B. C., & Manoharan, P. K. 2019, ApJ, 878, 130, doi: 10.3847/1538-4357/ab20c5

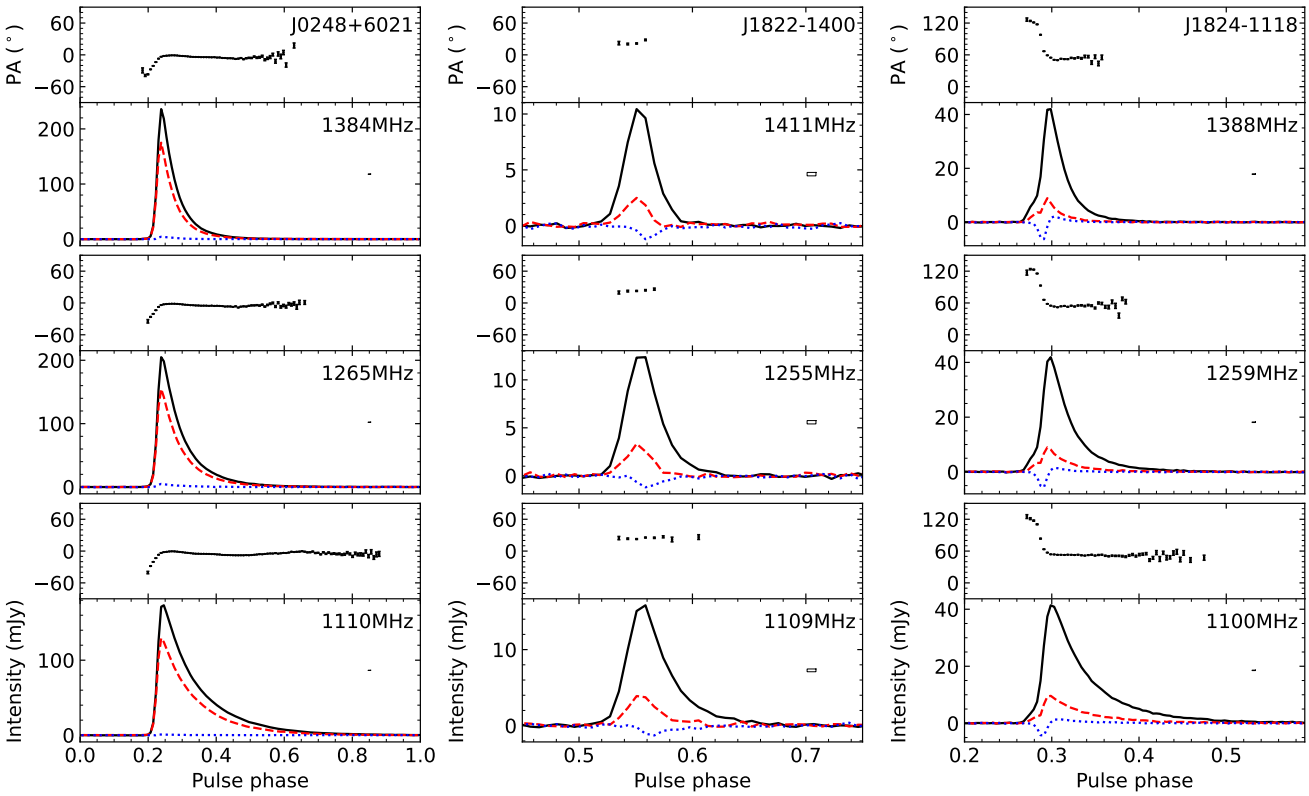


Figure A 4: Polarization profiles at 3 subbands of FAST observations for 82 scattered pulsars, including PSR J2052+4421 in Figure 1. Each profile has the total intensity in the solid line, linear polarization in the dashed line, and circular polarization in the dotted line. The band central frequency and the box for a bin size and $\pm 1\sigma$ are marked in the lower sub-panel. The polarization angles are plotted with error bars in the upper sub-panel. This figure is available in its entirety in the online supplementary material at ScienceDB https://doi.org/10.57760/sciencedb.j00167.0002b.

Krishnakumar, M. A., Mitra, D., Naidu, A., Joshi, B. C., & Manoharan, P. K. 2015, ApJ, 804, 23, doi: 10.1088/0004-637X/804/1/23

Kuz'min, A. D., & Izvekova, V. A. 1993, MNRAS, 260, 724, doi: 10.1093/mnras/260.4.724

Kuz'min, A. D., Kondrat'ev, V. I., Kostyuk, S. V., et al. 2002, Astronomy Letters, 28, 251, doi: 10.1134/1.1467260

Kuz'min, A. D., Losovskii, B. Y., & Lapaev, K. A. 2007, Astronomy Reports, 51, 615, doi: 10.1134/S1063772907080021

Kuzmin, A. D., & Losovsky, B. Y. 2007, Astronomical and Astrophysical Transactions, 26, 597, doi: 10.1080/10556790701610282

Lazarević, S., Filipović, M. D., Dai, S., et al. 2024, PASA, 41, e032, doi: 10.1017/pasa.2024.13

Lazio, T. J. W., Cordes, J. M., de Bruyn, A. G., & Macquart, J. P. 2004, NewAR, 48, 1439, doi: 10.1016/j.newar.2004.09.039

Lee, L. C., & Jokipii, J. R. 1975a, ApJ, 196, 695, doi: 10.1086/153458

—. 1975b, ApJ, 201, 532, doi: 10.1086/153916

Lewandowski, W., Dembska, M., Kijak, J., & Kowalińska, M. 2013, MNRAS, 434, 69, doi: 10.1093/mnras/stt989

Lewandowski, W., Kowalińska, M., & Kijak, J. 2015a, MNRAS, 449, 1570, doi: 10.1093/mnras/stv385

Lewandowski, W., Rożko, K., Kijak, J., Bhattacharyya, B., & Roy, J. 2015b, MNRAS, 454, 2517, doi: 10.1093/mnras/stv2159

Li, X. H., & Han, J. L. 2003, A&A, 410, 253, doi: 10.1051/0004-6361:20031190

Löhmer, O., Kramer, M., Mitra, D., Lorimer, D. R., & Lyne, A. G. 2001, ApJL, 562, L157, doi: 10.1086/338324

Löhmer, O., Mitra, D., Gupta, Y., Kramer, M., & Ahuja, A. 2004, A&A, 425, 569, doi: 10.1051/0004-6361:20035881

Lower, M. E., Dai, S., Johnston, S., & Barr, E. D. 2024, ApJL, 967, L16, doi: 10.3847/2041-8213/ad4866

Main, R., van Kerkwijk, M., Pen, U.-L., Mahajan, N., & Vanderlinde, K. 2017, ApJL, 840, L15, doi: 10.3847/2041-8213/aa6f03

Manchester, R. N., Hobbs, G. B., Teoh, A., & Hobbs, M. 2005, AJ, 129, 1993, doi: 10.1086/428488

Meyers, B. W., Tremblay, S. E., Bhat, N. D. R., et al. 2017, ApJ, 851, 20, doi: 10.3847/1538-4357/aa8bba

Nan, R. 2006, Science in China: Physics, Mechanics and Astronomy, 49, 129, doi: 10.1007/s11433-006-0129-9

Nan, R., Li, D., Jin, C., et al. 2011, International Journal of Modern Physics D, 20, 989, doi: 10.1142/S0218271811019335
Nice, D. J., Altiere, E., Bogdanov, S., et al. 2013, ApJ, 772, 50, doi: 10.1088/0004-637X/772/1/50
O'Brien, J. T., Johnston, S., Kramer, M., et al. 2008, MNRAS, 388, L1, doi: 10.1111/j.1745-3933.2008.00481.x
Ocker, S. K., & Cordes, J. M. 2026, ApJ, 1002, 3, doi: 10.3847/1538-4357/ae5825
Ocker, S. K., Cordes, J. M., & Chatterjee, S. 2020, ApJ, 897, 124, doi: 10.3847/1538-4357/ab98f9
—. 2021, ApJ, 911, 102, doi: 10.3847/1538-4357/abeb6e
Ocker, S. K., Cordes, J. M., Chatterjee, S., & Gorsuch, M. R. 2022, arXiv e-prints, arXiv:2203.16716. https://arxiv.org/abs/2203.16716
Oronsaye, S. I., Ord, S. M., Bhat, N. D. R., et al. 2015, ApJ, 809, 51, doi: 10.1088/0004-637X/809/1/51
Oswald, L. S., Karastergiou, A., Posselt, B., et al. 2021, MNRAS, 504, 1115, doi: 10.1093/mnras/stab980
Parent, E., Sewalls, H., Freire, P. C. C., et al. 2022, ApJ, 924, 135, doi: 10.3847/1538-4357/ac375d
Patil, S. S., Main, R. A., Fonseca, E., et al. 2026, ApJL, 997, L5, doi: 10.3847/2041-8213/ae2eb3
Pennucci, T. T., Possenti, A., Esposito, P., et al. 2015, ApJ, 808, 81, doi: 10.1088/0004-637X/808/1/81
Pushkarev, A. B., Brunthaler, A., Kovalev, Y. Y., et al. 2026, arXiv e-prints, arXiv:2602.06785. https://arxiv.org/abs/2602.06785
Pynzar', A. V., & Shishov, V. I. 2008, Astronomy Reports, 52, 623, doi: 10.1134/S1063772908080039
Ramachandran, R., Mitra, D., Deshpande, A. A., McConnell, D. M., & Ables, J. G. 1997, MNRAS, 290, 260, doi: 10.1093/mnras/290.2.260
Reid, M. J., Menten, K. M., Brunthaler, A., et al. 2019, ApJ, 885, 131, doi: 10.3847/1538-4357/ab4a11
Rickett, B. J. 1977, ARA&A, 15, 479, doi: 10.1146/annurev.aa.15.090177.002403
—. 1990, ARA&A, 28, 561, doi: 10.1146/annurev.aa.28.090190.003021
Scheuer, P. A. G. 1968, Nature, 218, 920, doi: 10.1038/218920a0
Sengar, R., Bailes, M., Balakrishnan, V., et al. 2023, MNRAS, 522, 1071, doi: 10.1093/mnras/stad508
Singha, J., Joshi, B. C., Krishnakumar, M. A., et al. 2024, MNRAS, 535, 1184, doi: 10.1093/mnras/stae2405
Slee, O. B., Dulk, G. A., & Otrupcek, R. E. 1980, PASA, 4, 100, doi: 10.1017/S1323358000018968
Smirnova, T. V., & Shishov, V. I. 2010, Astronomy Reports, 54, 139, doi: 10.1134/S106377291002006X
Spitler, L. G., Lee, K. J., Eatough, R. P., et al. 2014, ApJL, 780, L3, doi: 10.1088/2041-8205/780/1/L3
Staelin, D. H. 1970, Nature, 226, 69, doi: 10.1038/226069a0
Su, W. Q., Han, J. L., Wang, P. F., et al. 2023, arXiv e-prints, arXiv:2305.16754, doi: 10.48550/arXiv.2305.16754
Surnis, M. P., Joshi, B. C., McLaughlin, M. A., et al. 2019, ApJ, 870, 8, doi: 10.3847/1538-4357/aaee7f
Sutton, J. M. 1971, MNRAS, 155, 51, doi: 10.1093/mnras/155.1.51
Taylor, J. H., & Cordes, J. M. 1993, ApJ, 411, 674, doi: 10.1086/172870
van Straten, W. 2004, ApJS, 152, 129, doi: 10.1086/383187
van Straten, W., & Bailes, M. 2011, PASA, 28, 1, doi: 10.1071/AS10021
van Straten, W., Demorest, P., & Oslowski, S. 2012, Astronomical Research and Technology, 9, 237, doi: 10.48550/arXiv.1205.6276
Voûte, J. L. L., Kouwenhoven, M. L. A., van Haren, P. C., et al. 2002, A&A, 385, 733, doi: 10.1051/0004-6361:20020123
Wang, P. F., Han, J. L., Xu, J., et al. 2023, Research in Astronomy and Astrophysics, 23, 104002, doi: 10.1088/1674-4527/acea1f
Wang, S. Q., Wang, J. B., Hobbs, G., et al. 2020, ApJ, 897, 8, doi: 10.3847/1538-4357/ab9302
Wongphechauxsorn, J., Champion, D. J., Bailes, M., et al. 2023, arXiv e-prints, arXiv:2310.14008, doi: 10.48550/arXiv.2310.14008
Xu, J., Han, J., Wang, P., & Yan, Y. 2022, Science China Physics, Mechanics, and Astronomy, 65, 129704, doi: 10.1007/s11433-022-2033-2
Xu, S., & Zhang, B. 2017, ApJ, 835, 2, doi: 10.3847/1538-4357/835/1/2
Xue, M., Ord, S. M., Tremblay, S. E., et al. 2019, PASA, 36, e025, doi: 10.1017/pasa.2019.19
Yan, Y., Han, J. L., Zhou, D. J., et al. 2024, ApJ, 965, 25, doi: 10.3847/1538-4357/ad2e9c
Yan, Y., Wang, P. F., & Han, J. L. 2023, MNRAS, 523, 5207, doi: 10.1093/mnras/stad1775
Yao, J. M., Manchester, R. N., & Wang, N. 2017, ApJ, 835, 29, doi: 10.3847/1538-4357/835/1/29
Young, O., & Lam, M. T. 2024, ApJ, 962, 131, doi: 10.3847/1538-4357/ad1ce7
Zakharenko, V. V., Vasylieva, I. Y., Konovalenko, A. A., et al. 2013, MNRAS, 431, 3624, doi: 10.1093/mnras/stt470